# Hydrothermal Synthesis and Characterization of Nanocomposite Based on Chalcopyrite Nanostructures decorated on Hexagonal Boron Nitrides Nanosheets to Investigate the Electrochemical Sensing of NSCLC Biomarker

## A DISSERTATION REPORT

SUBMITTED IN PARTIAL FULFILMENT OF THE REQUIREMENTS FOR THE AWARD OF THE DEGREE

OF

MASTER OF SCIENCE

IN

**PHYSICS**

Submitted by:

**ARUN SAJI**

**(2K22/MSCPHY/05)**

Under the supervision of

**Prof. Nitin K. Puri**



## DEPARTMENT OF APPLIED PHYSICS

DELHI TECHNOLOGICAL UNIVERSITY

(Formerly Delhi College of Engineering)

Bawana Road, Delhi-110042

JUNE, 2024

## DEPARTMENT OF APPLIED PHYSICS

DELHI TECHNOLOGICAL UNIVERSITY

(Formerly Delhi College of Engineering)

Bawana Road, Delhi-110042

# <u>SUPERVISOR CERTIFICATE</u>

I hereby certify that the project dissertation titled "**Hydrothermal Synthesis and Characterization of Nanocomposite based on Chalcopyrite Nanostructures decorated on Hexagonal Boron Nitrides Nanosheets to Investigate the Electrochemical Sensing of NSCLC Biomarker**", by **ARUN SAJI (2K22/MSCPHY/05)** submitted to the **Department of Applied Physics, Delhi Technological University,** in complete fulfillment of the requirements for the award of grades of semester IV in Applied Physics, is a record of the project work carried out by the student under my supervision. To the best of my knowledge, this work has not been submitted, either partially or completely, for any degree or diploma at this university or elsewhere.

Place: New Delhi                                          **Prof. Nitin K. Puri**

Date:                                             Department of Applied Physics

                                                        Delhi Technological University

**DEPARTMENT OF APPLIED PHYSICS**

DELHI TECHNOLOGICAL UNIVERSITY

(Formerly Delhi College of Engineering)

Bawana Road, Delhi-110042

# ACKNOWLEDGEMENT

I would like to express my indebtedness and deepest sense of gratitude to my supervisor, Prof. Nitin K. Puri, Professor, Department of Applied Physics, Delhi Technological University for providing his incessant expertise, inspiration, encouragement, suggestions, and the opportunity to work under his guidance. I am grateful for the constant help and encouragement provided at every step of this project by the PhD scholars, Ms. Kanika Sharma and Mr. Anurag Bhandari of the Nanomaterials Research Laboratory (NRL), Department of Applied Physics, Delhi Technological University.

I am also grateful to all my family and friends for their invaluable support, care, and patience during this project. Lastly, I would like to thank Delhi Technological University for providing such a wonderful opportunity to work on this project and providing me with all the necessary facilities.

**ARUN SAJI**

**(2K22/MSCPHY/05)**

# CANDIDATE'S DECLARATION

I, **Arun Saji (2K22/MSCPHY/05)**, a student of M.Sc. Physics, hereby declares that the project dissertation titled, "**Hydrothermal Synthesis and Characterization of Nanocomposite based on Chalcopyrite Nanostructures decorated on Hexagonal Boron Nitrides Nanosheets to Investigate the Electrochemical Sensing of NSCLC Biomarker**" which is submitted by me to the **Department of Applied Physics, Delhi Technological University**, **Delhi** in complete fulfillment of the requirement for the award of the degree of Master in Science, is original and not copied from any source without proper citation. This work has not previously formed the basis for awarding any degree, Diploma Associateship, Fellowship, or other similar title or recognition.

Place: New Delhi                                          **ARUN SAJI**

Date:                                                          **(2K22/MSCPHY/05)**

# CONTENTS

# LIST OF FIGURES

# LIST OF TABLES

# LIST OF SYMBOLS

| Symbols | Abbreviations |
| --- | --- |
| h-BN | Hexagonal Born Nitride |
| TTMC | Transition Ternary Metal Chalcogenide |
| TMC | Transition Metal Chalcogenide |
| NSCLC | Non-Small Cell Lung Cancer |
| CEA | Carcinoembryonic Antigen |
| EPD | Electrophoretic Deposition |
| DPV | Differential Pulse Voltammetry |
| CV | Cyclic Voltammetry |
| EDC | 1-(3-dimethylamino-propyl)-3-ethylcarbodiimide hydrochloride |
| NHS | N-hydroxysuccinimide |
| BSA | Bovine Serum Albumin |
| IPA | Isopropanol |
| ITO | Indium Tin Oxide |
| EPD | Electrophoretic Deposition |
| XRD | X-ray Diffraction |
| SEM | Scanning Electron Microscopy |
| FT-IR | Fourier Transform Infrared Spectroscopy |
| UV-vis | Ultraviolet-Visible Spectroscopy |

# ABSTRACT

Nanocomposites play a pivotal role in the fabrication of extraordinary electrochemical sensing platforms as they possess high catalytic ability, good chemical stability, versatility, and ultra-high surface sites for accurate, selective probing of target analytes. Taking into consideration, copper ferrous sulfide ($CuFeS_2$, widely known as chalcopyrite), a promising candidate of ternary transition metal chalcogenide family (TTMC) that possesses good chemical stability, high carrier concentration, commendable adsorption ability, and high catalytic nature. Hexagonal Boron Nitride (h-BN) on the other hand is an inorganic layered material with notable properties such as excellent thermal and chemical stability, biocompatibility, and high surface adsorption compatibility. Yet, it lacks catalytic properties and electron transfer efficiency. In this work, a nanocomposite based on $CuFeS_2$-hBNNS was synthesized by one-pot facile hydrothermal synthesis, as an attempt to overcome the shortcomings of hBNNS. The properties of as-synthesized nanocomposite were investigated through XRD, SEM, FT-IR, and UV-visible spectroscopy. Further, the hydrolyzed indium tin oxide (ITO) glass substrates were used as the substrate for the electrophoretic deposition process (EPD), which was used to develop microelectrodes of $CuFeS_2$-hBNNS at low DC potential (20 V). Successive immobilization of the protein biomarkers associated with Non-Small Cell Lung Cancer (NSCLC), including Anti-CEA, BSA, and CEA, were carried out. Subsequently, cyclic voltammetry (CV) and differential pulse voltammetry (DPV) unravelled the diffusion-controlled process and the fruitful protein immobilization depicts the potentiality of $CuFeS_2$-hBNNS nanocomposite for electrochemical sensing of the targeted inoperable disease.

# CHAPTER-1: INTRODUCTION

Nanotechnology and nanomaterials have garnered substantial attention in recent years due to their remarkable properties and diverse applications across various fields. Various industries in the present era such as energy, textiles, agriculture, defence, healthcare, and so on are evolving due to the emergence of nanomaterials-driven technology that includes supercapacitors, sensors, point-of-care biosensors, surveillance systems, protective gear, smart fabrics, water purification systems, packaging, and more. This technology revolves around the manipulation and control of matter at an atomic scale and represents not only an incremental advancement but also a revolutionary leap in science and engineering. It promises to redefine the aspects of technology and industry by exploring and exploiting exceptional properties of materials that emerge at the nanoscale. It bridges the molecular and atomic worlds, where conventional laws of physics merge with quantum mechanics, endowing "quantum confinement" at the atomic and molecular levels. [1]. Nanomaterials, the foundational elements of nanotechnology, possess unique and remarkable mechanical, chemical, optical, and biological properties that are markedly different from those of their larger counterparts [2]. The exquisite chemical traits exhibited by the nanomaterials can be attributed to their high surface area and quantum effects which help them to be excellent catalysts [3, 4]. Due to their grain boundary-strengthening effects, physical qualities such as mechanical strength, magnetic properties, energy band gap, and thermal conductivity are also distinct from their bulk counterparts [5, 6]. Quantum confinement of the nanoparticle gives rise to unique optical phenomena such as size-dependent photoluminescence [7, 8]. Finally, due to their large surface area equipped with several binding sites, they play an instrumental role in biological fields making them much more effective and efficient than their bulk counterparts [9, 10].

Nanomaterials exhibit a wide range of properties that are influenced by their origin, structure, size, and chemical composition. Their physical, chemical, optical, and electrical properties are drastically altered by these factors, thereby impacting the performance of transducing devices used across various applications. Consequently, they are divided into various subclasses based on their: (1) Dimensionality and (2) Composition. The nanomaterials are categorized into four categories based on their morphology: (i) Zero (0-D), (ii) One (1-D), (iii) Two (2-D), and (iv) Three (3-D)

dimensional nanomaterials [2, 11]. Among the mentioned subcategories of nanomaterials, 2-D nanomaterials differ from the rest due to their high electron mobility, ease of functionalization, high surface area, flexibility, layer-dependent properties, commendable mechanical strength, and binding sites [12]. These unique properties make 2-D nanomaterials particularly interesting. Definition-wise, 2-D nanomaterials have two dimensions outside the nanoscale and one well within it (about 1-100 nm), indicating that we have one-way confinement, which gives rise to the supremacy of quantum effects that are impossible to ignore [13]. Further, the 2-D nanomaterials are classified into subcategories based on their composition as, organic, inorganic, and hybrid composite [14, 15]. The absence of carbon and hydrogen sets inorganic nanomaterials apart from organic layered materials. They are in turn made up of elements like sulfur, nitrogen, boron, and molybdenum. Due to their high chemical and thermal stability, a diverse range of electrical capabilities, and noteworthy mechanical strength, they have been employed in variegated spheres of applications [16, 17].

Among various different members of inorganic layered material family hexagonal boron nitrides (h-BN) is the most notable member. h-BN has earned the title "white graphene" because of its astonishing isomorphism with graphene. It consists of layers of hexagonally arranged boron and nitrogen atoms joined by $sp^2$ hybridization [18]. Recognized for having a large energy band gap (~ 5-6 eV) coupled with low chemical catalytic properties this substance has unfortunately not received enough attention for electrochemical uses. However, it is a promising candidate for use in various scientific domains due to its other intriguing qualities, which include a large surface area, superior chemical stability, inertness to oxidation with ease of functionalization, and an adjustable band gap [18, 19]. Hence, to fully exploit this eccentric material we need to overcome its shortcomings which can be done by coupling it with suitable materials.

Here, the fascinating family of Ternary Transition Metal Chalcogenides (TTMCs), a subclass of Transition Metal Chalcogenides (TMCs), emerges as a suitable candidate. As the name suggests each member of TTMC is made up of three elements: one is a chalcogenide, such as oxygen or sulfur, and the others are either metals or non-metals. The transition elements are those found in the d-block, such as copper, silver, and gold. The family's well-known qualities are good adsorption ability, chemical stability, high carrier concentration, high catalytic activity, and structural variety.

$CuFeS_2$, $CuAlS_2$, $CuInS_2$ are among the most intriguing members of this family [20, 21].

Within the TTMC family, $CuFeS_2$, widely referred to as chalcopyrite, garners significant attention due to its remarkable and distinguishable traits. This mineral, with its brassy yellow hue, exhibits a tetragonal crystal structure and is widely recognized for its metallic lustre and semi-conductive properties. This is because $CuInS_2$ extraction and processing have serious environmental impacts [22, 23] on the other hand $CuAlS_2$ have stability issues [24, 25], and hence their usage is limited. $CuFeS_2$ holds immense significance due to its extensive utilization across a wide range of industries. It is notably the most commonly used element in its family. Its applications are diverse and can be found in fields such as photo-catalysis, solar cells, energy storage, and battery technology. This versatile mineral plays a crucial role in advancing various technological and industrial processes. [26, 27]. This element stands out due to its exceptionally low optical bandgap and outstanding photo-catalytic effectiveness, making it an incredibly compelling choice for a wide range of applications. With its high catalytic activity, variable bandgap, low toxicity, and synergistic effects, it presents a wealth of promising opportunities. Moreover, its environmentally friendly nature warrants thorough exploration of its potential use in green energy sources [26, 27]. Previous research has demonstrated that nanocomposites have the potential to yield materials with vastly improved, enhanced, and customizable properties, thereby offering a broad range of practical applications across various industries [28, 30]. The versatile properties of nanocomposites make them indispensable in a wide range of applications, including automotive, batteries, electronics, medical field, and sensing. [31-35].

In the context of sensing inoperable ailments, nanocomposites have proved to be far superior to the conventional methods of diagnosis in terms of sensitivity, efficiency, and reliability [34, 35]. The researchers have extensively discussed the crucial role of nanocomposites in advancing electrochemical sensing technologies for detecting specific biomarkers associated with Non-Small Cell Lung Cancer (NSCLC). This is particularly noteworthy due to NSCLC being the most prevalent form of lung cancer, constituting more than 85% of all cases [36]. The potential implications of this research are vast, as improved detection methods could lead to earlier diagnosis and more effective treatment strategies for NSCLC patients [36]. Smoking [37], passive

smoking [38], prolonged exposure to radon [39, 40], asbestos [41], air pollution [42, 43], and genetic factors [44] are the most common risk factors of NSCLC. The clinical signs of NSCLC include explanatory weight loss, prolonged coughs, chest uneasiness, fever, clubbing of fingernails [45], and so on, which unfortunately are non-specific [46]. Due to such inconspicuous symptoms and expensive methods of diagnosis, it is normal for the patient to delay seeking medical treatment until it is too late [47].

The remarkable advancements in the field of molecular biology have paved the way for the discovery of biomarkers, which play a pivotal role in assessing the severity of various illnesses, with particular emphasis on cancer prognosis. These biomarkers are highly regarded by medical professionals worldwide due to their ability to provide valuable insights into the progression of diseases. Specifically, in the context of non-small cell lung cancer (NSCLC), carcinoembryonic antigen (CEA) has garnered attention as an exceptionally reliable biomarker for accurate diagnosis and monitoring of the disease's progression. This detailed information aids in developing personalized and effective treatment plans for patients, ultimately contributing to improved outcomes and quality of care. It was observed that the levels of CEA in the body fluids of a typical person were maintained at 5 ng/ml, which is treated as a cut-off concentration [48], and with the onset of the disease, the levels rose, as high as to its 70 % of its normal levels [49, 50].

In our study we synthesized a unique nanocomposite by combining h-BN with $CuFeS_2$, leveraging its straightforward functionalization process. This innovative approach allowed us to overcome the limitations of h-BN, such as its large energy gap and low catalytic activities, resulting in a nanocomposite with vastly improved characteristics. Through the enrichment of valence states and the utilization of notable synergistic effects from copper and iron, $CuFeS_2$ significantly enhanced the catalytic nature of h-BN, leading to a drastic reduction in the energy band gap. This strategic coupling of h-BN with chalcopyrite has given rise to a new class of nanocomposite with remarkably enhanced electrocatalytic activity. Our comprehensively discussed various physical characterization techniques to confirm nanocomposite was successfully synthesized using a simple one-pot hydrothermal route. Subsequently, the fabricated nanocomposite was deposited onto indium tin oxide (ITO) substrates through electrophoretic deposition. The electrochemical characteristics of the electrodes were thoroughly analyzed using Cyclic Voltammetry (CV) and Differential Pulse Voltammetry (DPV) studies.

# CHAPTER 2: EXPERIMENTAL SECTION

## 2.1 Importance of Hydrothermal Route

Hydrothermal synthesis stands out as a cornerstone in the realm of nanomaterial fabrication, offering a remarkable avenue for tailoring the properties of materials at the nanoscale with unprecedented precision and control. Rooted in the principles of aqueous chemistry under elevated temperature and pressure conditions, hydrothermal synthesis harnesses the transformative power of water as both a solvent and a reactant to devise the assembly of nanoscale architectures with tailored functionalities and morphologies [51, 52]. The captivating features of hydrothermal synthesis include its ability to serve as a versatile and robust platform for the creation of a diverse array of nanomaterials, ranging from metal oxides and sulfides to carbon-based structures and beyond. By modulating reaction parameters such as temperature, pressure, pH, and precursor composition, the researchers have focussed a profound influence over the nucleation, growth, and crystallization processes that underpin the formation of nanomaterials, thereby bestowing precise control over their size, shape, surface chemistry and crystallinity [53-55].

Beyond its unparalleled control over material properties, hydrothermal synthesis offers distinct advantages over the other conventional synthesis methods. It operates at moderate temperatures and pressures, rendering it energy-efficient and amendable to large-scale productions, while its aqueous milieu promotes homogenous reactions and enables facile incorporation of dopants or functionalization agents [55]. Moreover, the closed, pressurized environment of hydrothermal reactors fosters the synthesis of materials with enhanced purity and uniformity, as well as the realization of metastable phases or exotic nanostructures that may be elusive under ambient conditions [53-55]. Hence, due to its versatility and efficacy, hydrothermal synthesis finds widespread applications across diverse fields, spanning catalysis, energy storage, environmental remediation, biomedicine, and beyond [56, 57]. From high-performance electro-catalysts for fuel cells to drug delivery carriers with precise control over drug release kinetics, the impact of hydrothermal synthesis reverberates across a spectrum of technological frontiers, propelling advancements that promise to reshape industries and redefine the boundaries of scientific exploration [56, 57].

Despite these advantages, hydrothermal synthesis also suffers from certain shortcomings such as longer reaction times and the need for specialized equipment. Additionally, controlling reaction conditions precisely can be challenging, and the optimization of parameters may be required for each specific material system [58].

## 2.2 Materials Used

Copper chloride dehydrate ($CuCl_2.2H_2O$) was procured from Central Drug House (CDH), whereas ferric chloride ($FeCl_3$) and thiourea were purchased from Thermo Fisher. Sigma Aldrich provided the bulk boron nitride powder(BN), 1-(3-(dimethylamino)-propyl)-3-ethylcarbodiimide hydrochloride (EDC), N-hydroxysuccinimide (NHS), bovine serum albumin (BSA), and monoclonal CEA antibody and antigen. Chemical reagents that were used in the whole experimental procedure were acquired from Fisher Scientific which included hydrazine ($N_2H_4H_2O>99\%$) and isopropanol (IPA, $(CH_3)_2CHOH$). Also, the acetonitrile ($CH_3CN$) and ethanol ($C_2H_5OH$) were bought from Merck. All the purchased chemicals and reagents were discovered to be high purity and were directly used without further purification.

## 2.3 Synthesis of CuFeS₂ Nanoparticles

For the synthesis of $CuFeS_2$ nanostructures, we followed an in-situ hydrothermal procedure which was mentioned in great detail in the works [59]. Accordingly, we prepared a solution of cupric chloride dihydrate and ferric chloride each of 0.15 M. Then the solutions were stirred vigorously for 10 mins with the help of a magnetic stirrer. Following this, a solution of thiourea of 0.30 M was added to the mixture after which the solution was then subjected to magnetic stirring for an hr. For the conduction of a successful hydrothermal procedure, the solution is transferred to a 100 ml Teflon autoclave and then kept the same in an oven at 200 °C for 10 hrs. Subsequently, the products so obtained were thoroughly washed with DI and centrifuged. After this, the yield was dried with the help of a vacuum oven at 60 °C for approximately 25 hrs. At the end of 25 hrs, the products were grinded and were annealed at 300 °C for an hour at a rate of 3 °C/min. **Fig. 1** depicts the synthesis procedure that was followed for the fabrication of the $CuFeS_2$.
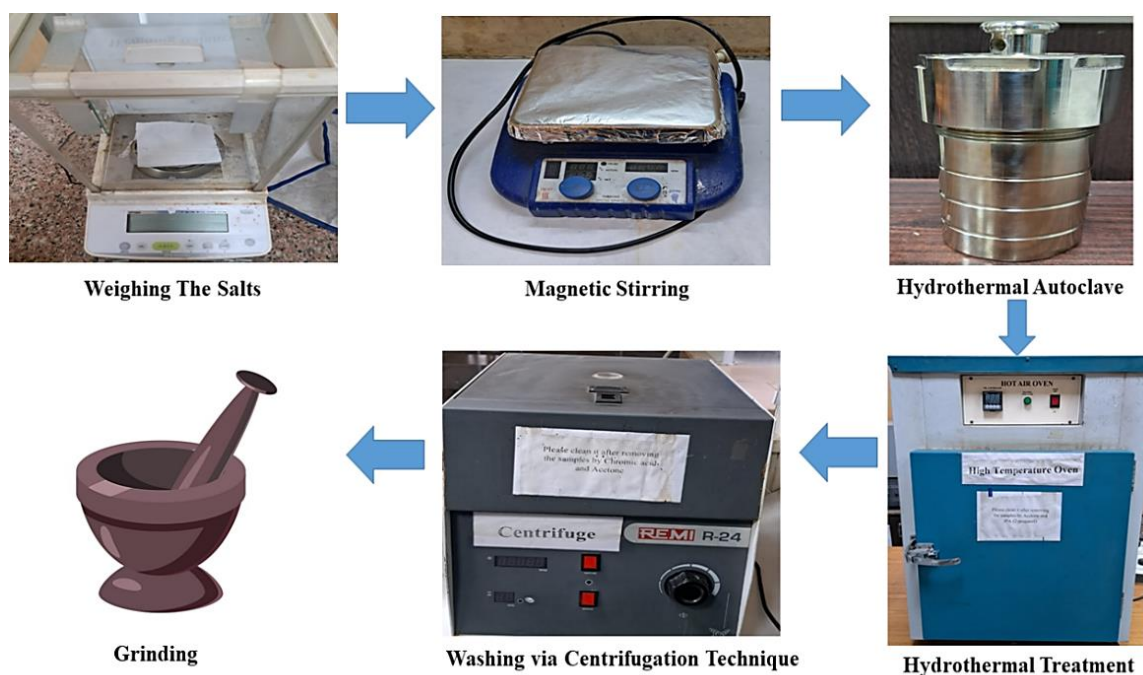
**Figure 1**: **Pictorial representation of hydrothermal synthesis of CuFeS$_2$ nanoparticles.**

## 2.4 Synthesis of the CuFeS$_2$-hBNNS Nanocomposite

Nanocomposite are the materials that combine nanoparticles with bulk matrix materials like metal, polymer and so on in order to improve their properties. In this work we enhanced the electrocatalytic efficiency of hBNNS by synthesizing a nanocomposite that decorates CuFeS$_2$ nanoparticles over hBNNS nanosheets. Interestingly, h-BN exhibits isostructural properties to graphene thereby exhibit immense potential in biosensing applications. Whereas, CuFeS$_2$ is a potential inorganic layered material that can efficiently tune the properties of hBNNS.To synthesize the proposed nanocomposite we resorted to in situ synthesis which involves the generation of nanaoparticles within the matrix during the composite formation process. Hence, for the fabrication of the nanocomposite, equal amounts of the synthesized CuFeS$_2$ and Bulk h-BN were ultrasonicated individually in 10 ml of isopropyl alcohol for an hr. Then the solutions were mixed at the end of the procedure. Then, to the above solution, 10 ml of deionized water (DI) was added and stirred for another half an hr. Again for the conduction of the hydrothermal route, the solution was transferred to a 100 ml Teflon autoclave. The autoclave was sealed in a stainless steel autoclave and then kept in the oven at 130 °C for a period of 4 hrs. Then the products were grinded and thoroughly washed with DI. Finally, the products were

annealed at 300 °C for an hr at a rate of 3°C/min. **Fig. 2** illustrates the one-pot hydrothermal synthesis followed for the successful fabrication of the nanocomposite, i.e., CuFeS$_2$-hBNNS
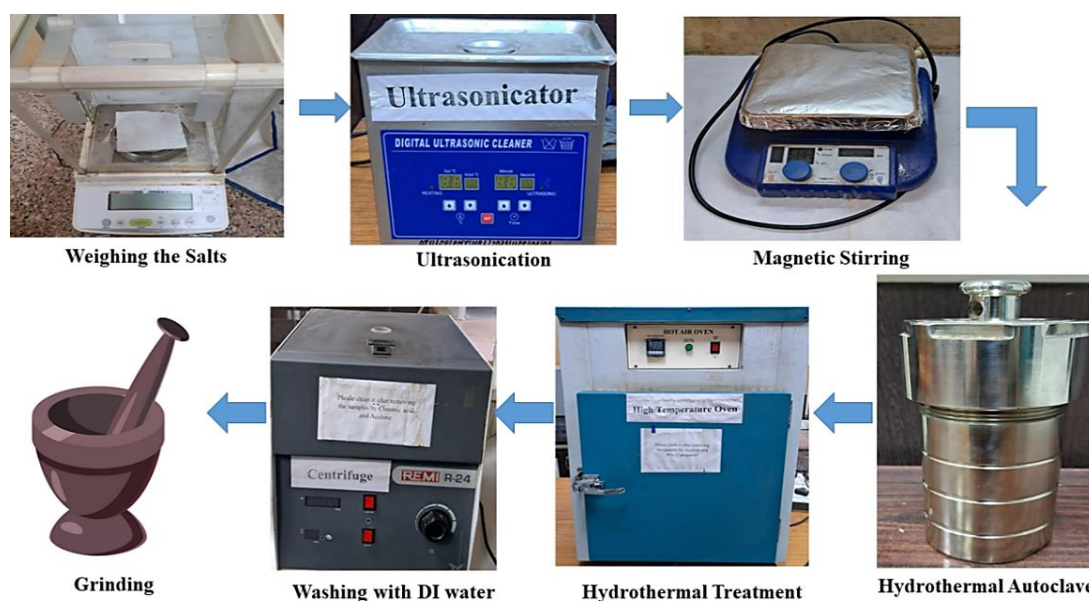


**Figure 2**: **Pictorial representation of the hydrothermal synthesis of the CuFeS$_2$-hBNNS nanocomposite.**

## 2.5 Fabrication of the Immunoelectrodes for the Electrochemical Detection of CEA

The electrophoretic deposition (EPD) approach was used to deposit the nanocomposite onto the indium tin oxide (ITO) slides, following the entire procedure indicated [60]. ITO electrodes are used because of their excellent conductivity, large potential window, steady electrochemical response, facile scaling, and cost-effectiveness [61]. Before deposition, the ITO electrodes went through hydrolysis. The electrodes were extensively hydrolyzed with ammonia, hydrogen peroxide, and DI water in a 1:1:5 ratio (volume). Deionized water was used to ensure that the hydrolysis process reaction occurs in a clean and controlled environment. Since it is free of ions and other impurities, which could interfere with the hydrolysis process or introduce contaminants to the ITO slides [62, 63]. By using deionized water, we make sure that we achieve reproducible results with minimal background noise [64]. Hydrogen peroxide is used as an oxidizing agent in the hydrolysis process of ITO slides. It helps in removing organic contaminants and surface residues from the surface, preparing it for matrix deposition. It promotes the formation of hydroxyl groups on the surface of

the slides during the hydrolysis reaction [65]. Ammonia is employed in the hydrolysis process as a base to adjust the pH of the solution. Controlling pH is crucial for optimizing the hydrolysis reaction and promoting the formation of hydroxyl groups on the surface of the ITO slides and ensures the successful fostering the matrix [66].

The process of hydrolysis can be described as an instrumental course of treatment to activate the radical groups on the electrodes. In the present context of ITO slides, this involves treating the surface of the slides with a strong acid or base, thus modifying the surface chemistry of ITO slides by creating hydroxyl (-OH) groups on the surface. These hydroxyl groups play a very significant role in fostering the matrix ($CuFeS_2$-hBNNS) onto the ITO slides, as they provide potential reactive binding sites for the successful immobilization of the matrix that are pivotal for biosensing applications [67].

Accordingly, the prepared nanocomposite was then suspended in acetonitrile at a concentration of 0.5 mg/mL Following that, a suspension of magnesium nitrate ($MgNO_3$) was developed using acetonitrile and ultrasonically treated for an hr to create a colloidal solution equivalent to the previously developed suspension of the nanocomposite. We made use of acetonitrile for the film formation onto ITO slides for many reasons. Firstly, acetonitrile offers high dispersibility for many organic and inorganic materials ensuring the solvent is versatile, as a result, a very thin film is formed [68]. Secondly, acetonitrile is very compatible with ITO slides and does not readily react with the surface, ensuring the integrity and conductivity of the ITO layer are maintained during the film deposition process [68]. Compatibility is vital for preserving the functionality of the slides. Also, the low surface tension of acetonitrile facilitates the formation of uniform and smooth films on the surface of the slides [68]. This property ensures minimal defects and good coverage of the substrate, leading to enhanced film quality and performance in biosensing applications.

A small amount of the produced $MgNO_3$ was then added to the nanocomposite solution to ensure that the nanocomposite securely bonds to the electrode surface throughout the EPD process. As a result, the above-mentioned homogeneous suspension of $CuFeS_2$-hBNNS was placed in a glass beaker comprising of 2 electrode system. The positive terminal of the EPD setup was connected to the platinum electrode, whereas the negative electrode was connected to the copper electrode. Then,

the pre-hydrolyzed ITO slides (3 cm x 1 cm) was mounted on the copper electrode for film deposition. Uniform deposition of the CuFeS$_2$-hBNNS (1 cm x 1 cm) onto the ITO electrode was attained at a DC voltage of 20 V as shown in **Fig. 3**. The choice of MgNO$_3$ to be used as a binding agent for the film formation is attributed to several advantageous reasons. The high solubility of MgNO$_3$ in water makes it easy to prepare homogenous precursor solutions for film deposition processes [68]. By adjusting parameters such as precursor concentration, deposition technique, and heat treatment conditions, researchers can tailor the properties of the deposited films to meet specific requirements for biosensing applications.
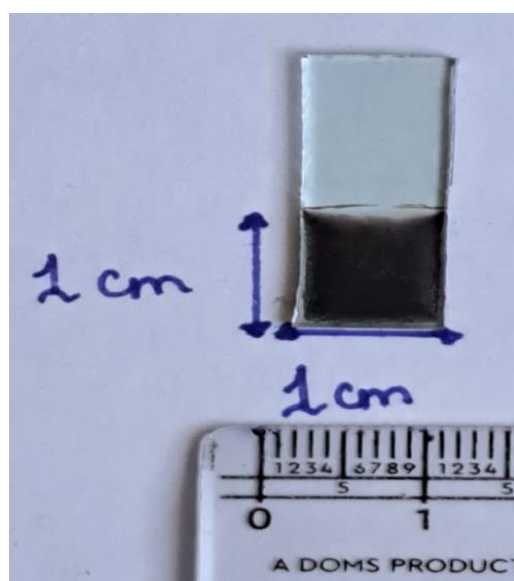


**Figure 3**: **EPD film comprising of CuFeS$_2$-hBNNS nanocomposite on ITO slide.**

Following at room temperature (25 °C), CuFeS$_2$-hBNNS/ITO electrodes were immobilised with protein biomolecules, and the modified immunoelectrode underwent comprehensive electrochemical examination. To begin, a stock solution of monoclonal Anti-CEA (50 µg/ml) diluted in pH 7.4 along with EDC (0.2 M) and NHS (0.05 M) in a 2:1:1 ratio to operate as an activator and stabilizer, respectively. Then 20 µL of CEA antibodies were mounted onto the unaltered film of CuFeS$_2$-hBNNS. The immunoelectrode was further evolved by adding 10 µL of BSA, resulting in the electrode composition BSA/Anti-CEA/CuFeS$_2$-hBNNS/ITO. The addition of BSA was required to rectify the alignment of the adsorbed Anti-CEA and prevent the contribution of all those Anti-CEA that were not adsorbed perpendicular to the electrode. Finally, 10 µL of CEA was applied to the BSA/Anti-CEA/CuFeS$_2$-hBNNS/ITO electrode.

# CHAPTER-3: CHARACTERIZATION

## 3.1 MATERIAL CHARACTERIZATION

### 3.1.1 X-Ray Diffraction

X-ray diffraction (XRD) stands out as a critical technique used worldwide to validate compound synthesis [69]. Solid-state compounds fall into two categories: crystalline and amorphous. When X-rays interact with solid atoms, they are deflected, producing a diffraction pattern. This pattern is a result of the interference of waves emitted by atoms at different positions. Constructive interference occurs when the atomic structure is ordered, while destructive interference occurs when it is not. The periodic atomic structure of crystals is intricately linked to their diffraction patterns. Diffraction occurs at small angles when there is a periodic atomic arrangement with long repeated distances, and at high angles when the distances are short. The intensity of diffraction peaks reveals the atomic location and number within the cell, while the position of the diffraction peaks determines the size and shape of the unit cell [69-71].
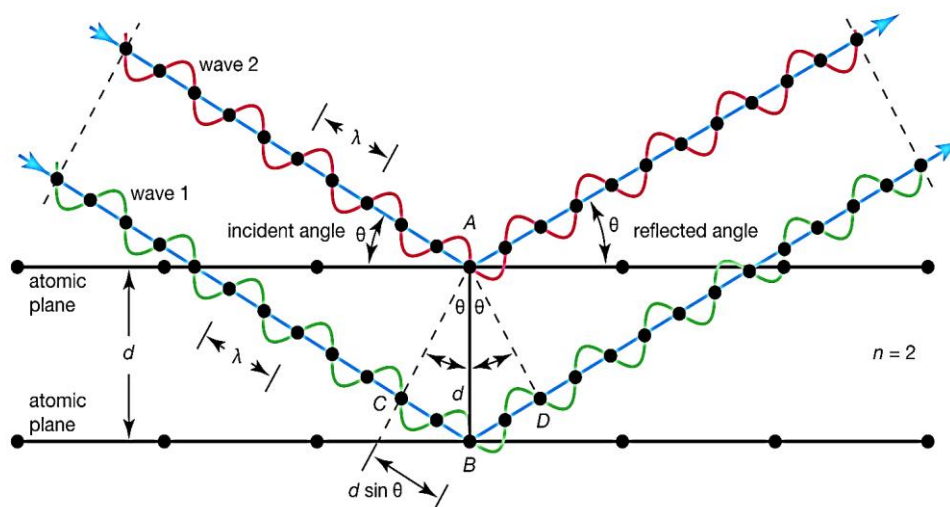


**Figure 4**: **Physical mechanism of the X-ray diffraction [reprinted from Jung et al., 72]**

According to Bragg's analysis (**Fig. 4**), crystals are arranged in atomic planes (lattice planes) whose miller indices are given as [hkl] with a separation of d, wherein d is the inter-planar spacing. The Bragg's diffraction requirement for constructive interference is met when the path difference lengths equal $n\lambda$, which can be expressed mathematically as follows:

$$2d\sin\Theta = n\lambda \qquad (1)$$

Where d is the inter-planar spacing between two atomic planes

Θ is the diffracting angle

n is the order of the diffraction (only integral values)

λ is the wavelength of the incident light

Hence **eq. (1)** relating the wavelength of the radiation with the angle of diffraction which can be experimentally observed will help us to deduce the unique set of interplanar spacing which helps us to correctly identify the compounds. The diffracted rays are collected and accounted for, and then subsequently these diffraction peaks are converted to the interplanar distances [70, 71].

A standard X-ray diffractometer is composed of three key elements: an X-ray tube, a sample holder, and an X-ray detector [69]. Electrons are accelerated in the cathode tube towards the sample, producing characteristic spectra when they have sufficient energy to probe the inner electrons [70]. The sample and the detector are rotated simultaneously to direct collimated rays onto the sample, with the detector recording the diffracted rays. Notable intensity is only generated and recorded when constructive interference occurs. These intensity recordings are then processed to generate the spectra [69, 70].

### 3.1.2 Scanning Electron Microscopy (SEM)

A scanning electron microscope utilizes a focused beam of electrons to produce detailed images of the sample under study, offering valuable insights into its composition and size [73]. SEM represents a significant advancement over light microscopes, providing superior magnification and resolving power to visualize the world at a smaller scale with exceptional clarity. Moreover, the SEM's high-voltage (around 50 kV) tungsten lamp serves as the radiation source, employing electromagnetics to focus the electrons [73-75].

The working principle of SEM is as follows [74, 75]. The produced electron beam from the tungsten source lamp is accelerated towards the target with the help of the application of high positive voltage. Following this, the beam is confined and focussed with the help of an electromagnetic lens which uses a magnetic field and metal apertures to produce a monochromatic beam of highly focused electrons. Subsequently, these electrons interact with the sample under study which produces an

output signal from which vital information about surface topography, composition, and other properties can be communicated by constructing images from these signals.
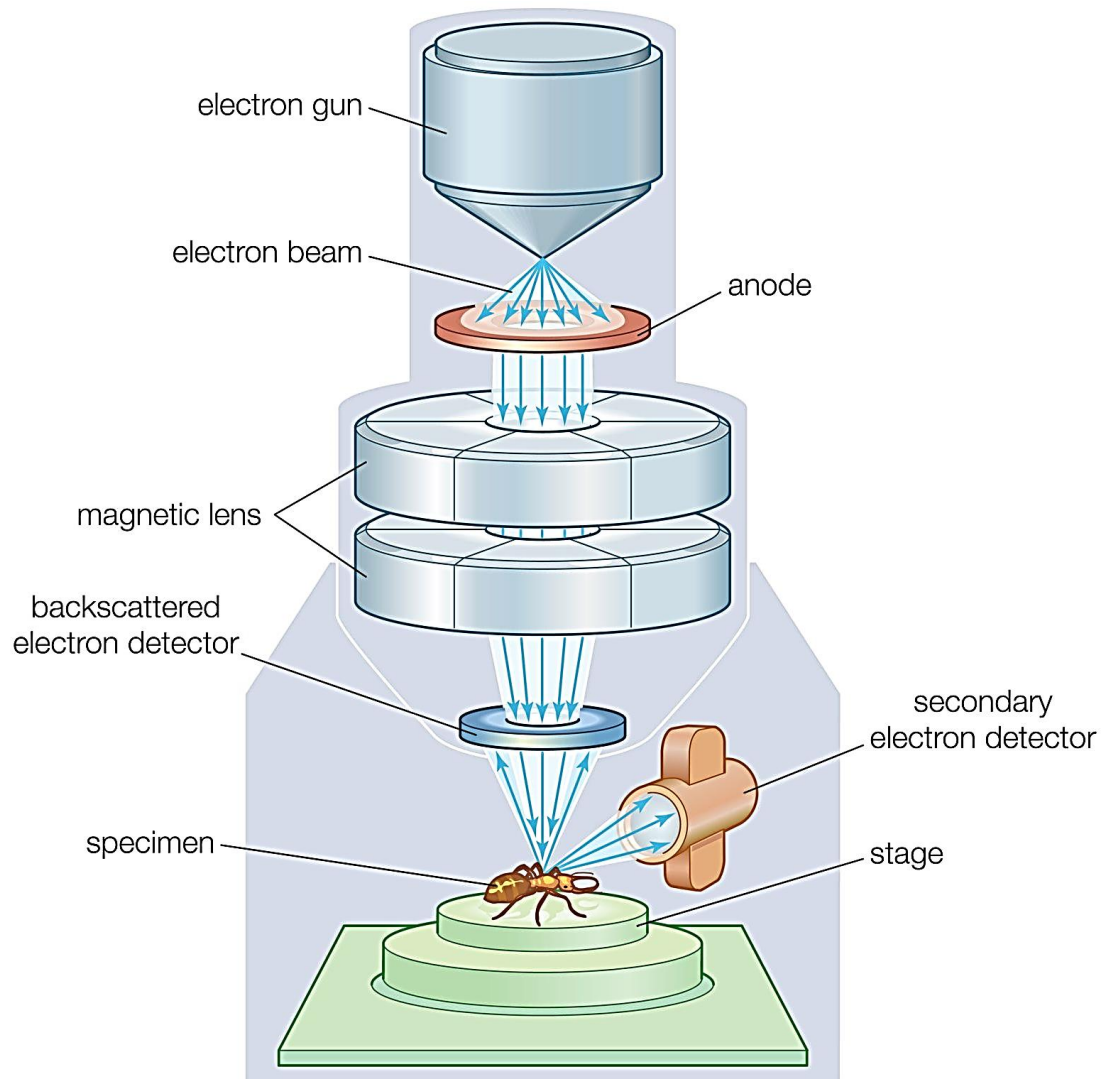


**Figure 5**: **Scanning Electron Microscope components and their working [reprinted from William et al., 76]**

SEM is extensively used to study the microstructure, composition, and defects of materials like metals, ceramics, polymers, and composites [73]. It plays a crucial role in characterizing nanoparticles, nanostructures, and nanomaterials, aiding research and development in nanotechnology. SEM provides high-resolution imaging of biological specimens such as cells, tissues, and microorganisms, contributing to advances in biology, medicine, and biotechnology. The following are the notable advantages and disadvantages [73-75]:

**Advantages**:

1. **High Resolution**: SEM offers superior resolution compared to optical microscopes, allowing visualization of fine surface details. Typically, optical microscopes have a diffraction limit of around 200 nm, whereas SEM resolutions are in the range of 1-10 nm

2. **Depth of Field**: It provides a large depth of field, enabling clear imaging of three-dimensional structures without any sample preparation. This is due to the nature of electron optics. This means that more of the specimen can be kept in sharp focus at the same time.

3. **Elemental Analysis**: SEM coupled with energy-dispersive X-ray spectroscopy (EDS) allows for elemental analysis, identifying the chemical composition of samples. Hence, they are equipped with additional detectors such as energy-dispersive X-ray spectrometers.

4. **Magnification Range**: SEM offers a wide magnification range, from tens to hundreds of thousands of times, accommodating various sample sizes and types. It offers magnification often exceeding 100000x, as compared to 1000-2000x of an optical microscope.

5. **Non-destructive**: SEM is a non-destructive technique, meaning samples can be imaged without altering their structure or composition.

**Disadvantages:**

1**. Complexity**: Operating SEM requires specialized training and expertise due to its complex instrumentation and techniques. The process of aligning the electron beam, adjusting the vacuum system, and interpreting the results is complex.

2. **Vacuum Requirement**: Samples must be placed in a vacuum chamber, which may limit the analysis of certain materials or biological specimens. Biological specimens, for example, need special preparation techniques which may change their natural state.

3. **Limited Depth Information**: SEM provides surface imaging and lacks depth information, requiring complementary techniques for three-dimensional analysis.

4**. Cost**: SEM equipment and maintenance can be costly, making it less accessible for smaller laboratories or academic institutions. It's expensive both in terms of initial purchase and maintenance costs

In conclusion, SEM is a versatile and powerful tool for surface imaging and analysis, offering high resolution and a wide range of applications across scientific disciplines and industries. Despite its complexity and limitations, its advantages make it indispensable for research, quality control, and technological advancement.

### 3.1.3 Fourier Transform Infrared Spectroscopy (FT-IR)

Fourier Transform Infrared Spectroscopy is one of the most effective material characterization methods. Its roots are deeply ingrained in the molecule's distinct vibrational spectrum. Furthermore, the infrared spectra assist us in doing both qualitative and quantitative examination of the material, with the depth of the peak depicting the amount of the required component in the material [77].

The initial infrared spectrometers relied on the dispersion of light, utilizing prisms or diffraction gratings to separate individual light frequencies. These frequencies were then individually passed through the sample, and the detector analyzed the energy content of each frequency after passing through the sample, resulting in a plot of transmitted light intensity versus frequency. However, this method was hindered by slow scanning speeds. Fourier transform infrared (FT-IR) spectroscopy has emerged as one of the most widely used characterization techniques due to its non-destructive nature, high optical throughput, enhanced sensitivity, and faster scanning speeds. FTIR devices are user-friendly, with mechanical simplicity and no need for external calibration [77]. Potassium Bromide (KBr) pellets were commonly used due to their opaque nature in the desired wavelength or spectrum range [77]. For our FTIR analysis, we utilized PerkinElmer's Spectrum Two Spectrometer.

A typical FTIR spectrometer consists of three key components: a broadband infrared light source, an interferometer, and a detector. **Fig. 6** illustrates the working and design of the FT-IR spectrometer The radiation source emits infrared radiation, which is split into two parts by the beam splitter. One part goes to the movable mirror, and the other to the stationary mirror. Reflected rays are directed towards the sample, absorbed, and then recorded by the detector. Applying the Fourier transform using a computer produces spectra showing the intensity of transmitted light as a function of wavenumber. The resulting FTIR spectrum offers valuable insights into the functional groups present in the sample's molecules. Each peak or band in the spectrum corresponds to specific vibrational modes of chemical bonds within the sample. By

comparing the sample's spectrum to reference spectra or databases, analysts can identify compounds and elucidate their chemical structure. FTIR spectroscopy is applied across various fields, including pharmaceuticals, polymers, environmental analysis, forensic science, and materials science, for qualitative and quantitative analysis, monitoring chemical reactions, and identifying unknown substances.
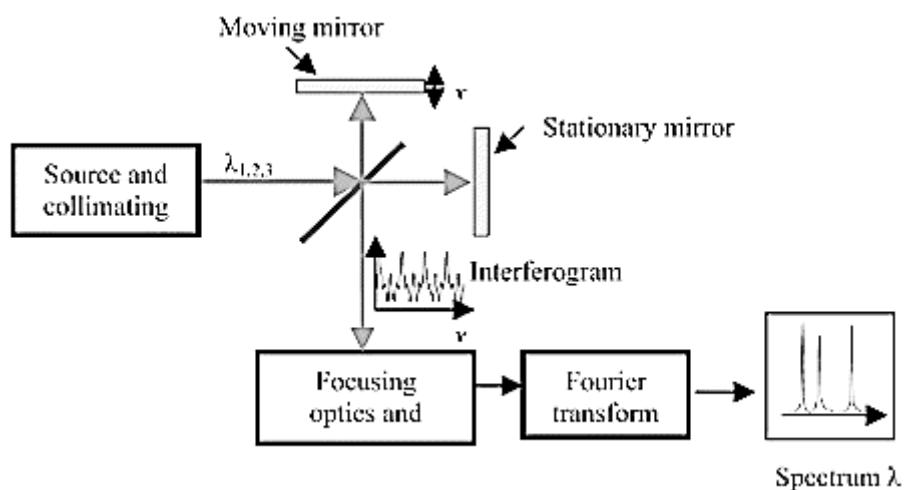


**Figure 6**: **FT-IR spectroscopy mechanism [reprinted from Saptari, 78]**

The following are the notable advantages of Fourier Transform Infrared Spectroscopy (FTIR) as stated in the reliable sources [79]:

1. **High Sensitivity**: FTIR offers high sensitivity, allowing the detection of small amounts of sample material.

2. **Wide Applicability**: It can analyze various types of samples including solids, liquids, and gases, making it versatile.

3. **Rapid Analysis**: FTIR provides rapid data acquisition, enabling quick analysis of samples, as it captures the entire band of wavelengths simultaneously.

4. **Quantitative Analysis**: It allows for quantitative analysis of sample components, facilitating accurate determination of concentrations.

5. **Non-destructive**: FTIR is a non-destructive technique, preserving the integrity of samples for further analysis.

The noticeable disadvantages of Fourier Transform Infrared Spectroscopy (FTIR) techniques are listed as follows [80]:

1. **Sample Preparation**: Some samples require preparation techniques such as grinding, pressing, or dilution, which can be time-consuming and may alter the sample's properties.

2. **Instrument Cost**: High-quality FTIR instruments can be expensive to acquire and maintain, limiting accessibility for smaller laboratories or institutions.

### 3.1.4 UV-Visible Spectroscopy

Ultraviolet spectroscopy is a powerful optical characterization technique that leverages light in the visible and ultraviolet regions to identify and quantify light-absorbing substances. When molecules or ions in a solvent are exposed to ultraviolet and visible light, they undergo electronic transitions, leading to significant changes in their electronic states. It stands as a crucial tool in the realm of optical characterization, offering precise and reliable analyses of light-absorbing substances This technique is governed by two fundamental laws: Lambert's law and Beer's law. According to Beer's law, the light-absorbing capability of a solute in a solvent is directly proportional to the solute's concentration, although deviations are observed at higher concentrations due to vibrational effects. Lambert's law states that each layer of the absorbing media of equal thickness will absorb an equal amount of light passing through it. When a beam of monochromatic light of intensity Io falls on a sample with concentration 'c' and sample length 'd', both laws can be combined into a single expression given as **eq. (2)**:

$$\log_{10} \frac{Io}{I} = Kcd \qquad (2)$$

**Where Io represents the intensity of the incident beam of light,**

**I represent the intensity of the transmitted light,**

**K is the constant of proportionality dependent upon the absorbing substance,**

**c is the concentration of the sample in the given solvent,**

**d is the distance traversed by the light through the cuvette**

This particular physical method is known for its versatility, ease of use, sensitiveness, reliability, correctness, and cost-effectiveness [81].

The principle of operation of the spectrometer is as follows, firstly light belonging to a specific range of wavelength is made to pass through the cuvette containing the sample and consequently, is made to fall onto a photoelectric cell which converts the radiant energy to electrical energy which can be fruitfully measured by a galvanometer [81]. Hence physically it generates the absorbance spectra of the sample under study. Beer Lambert's law is stated as **eq. (3)**:

$$A = \varepsilon bc \tag{3}$$

**Where A is the absorbance of the sample,**

**$\varepsilon$ is the absorptivity of the sample**

**b is the path length travelled by the light in the cuvette**

**c is the concentration of the solute in the solvent**

A typical UV-Vis spectrometer consists of the following components as pictorially depicted in **Fig. 7**:

**1.     Source:** The light source provides a stable and continuous spectrum of UV light. Xenon and Deutrium lamp are commonly employed for this purpose.

**2.     Filters and Monochromators:** These are used to isolate specific wavelengths of light from the continuous spectrum of light produced by the source. It consists of prisms or diffraction grating for separating the light into its component wavelengths.

**3.     Sample Compartment:** It houses the cuvette which is typically made up of quartz or another material transparent to UV light. It aligns the cuvette with the path of light.

**4.     Detector:** The detector measures the intensity of light that passes through the sample. Common detectors include photomultiplier tubes and photodiodes, which convert the transmitted light into an electrical signal**.**

**5.     Recorder:** It records the electrical signal from the detector and converts it into a readable format. It displays the absorbance or transmittance as a function of wavelength**.**
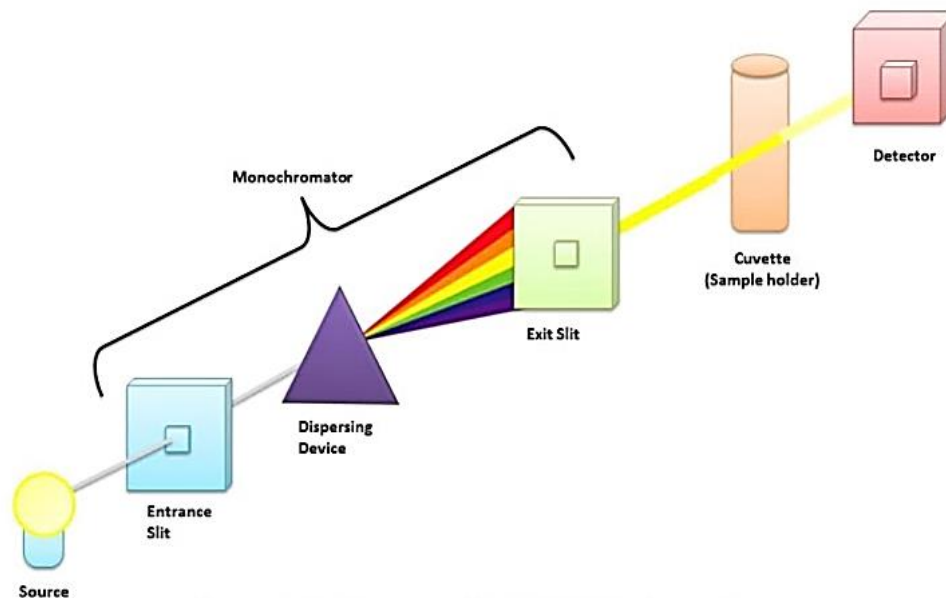
**Figure 7**: **A simple representative diagram of a UV-visible spectrometer [reprinted from Mukadam et al., 82]**
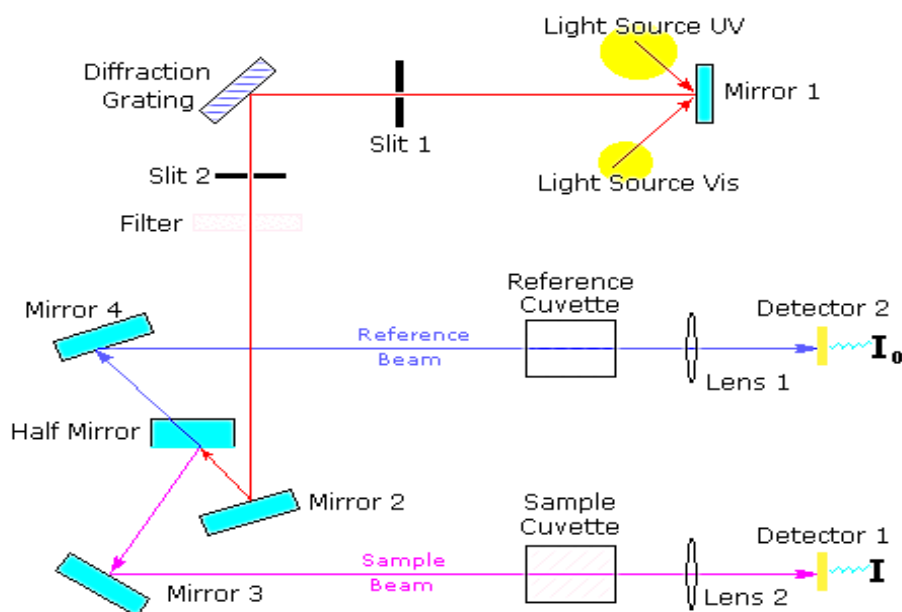


**Figure 8**: **Working of a typical UV-Visible spectrometer [reprinted from majeed, 83]**

As shown in **Fig. 8** the working of a common UV-Vis spectroscopy consists of splitting of light with the help of diffraction grating, which passes through the filter to get a collimated beam of light. Next, with the help of a mirror and a half-polished mirror, we split the beams into two parts which consequently made to pass through the reference sample and the sample cuvette. After this, the collected intensity is produced to give the absorption spectra.

19

The applications of UV-vis spectroscopy include the identification of contaminants, structural classification of organic compounds, quantitative, qualitative, and chemical analysis, and deviations from Beer- Lambert's law [81].

## 3.2 ELECTROCHEMICAL STUDIES

The complete electrochemical study was conducted on a three-electrode system consisting of a working electrode, reference electrode, and counter electrode. We have used a three-electrode system, as when we do measurements in the two-electrode system there is an addition of an intrinsic resistance which introduces errors that can't be accounted for accurately. The working electrode was modified immunoelectrode $CuFeS_2$-hBNNS/ITO, the reference electrode was Ag/AgCl and the counter electrode was the Platinum wire. The choice of the reference electrode was the basis of its high work function, and chemical inertness so that it does not interfere with the reactions [84], and hence can be used as a reference for voltage and current measurements. We chose platinum wire as the counter electrode due to its great electrical conductivity, comparatively low work function, and chemical inertness [85]. The main purpose of a counter electrode is to complete the circuit without giving out any foreign chemical products. Hence this fits the choice of the electrodes.
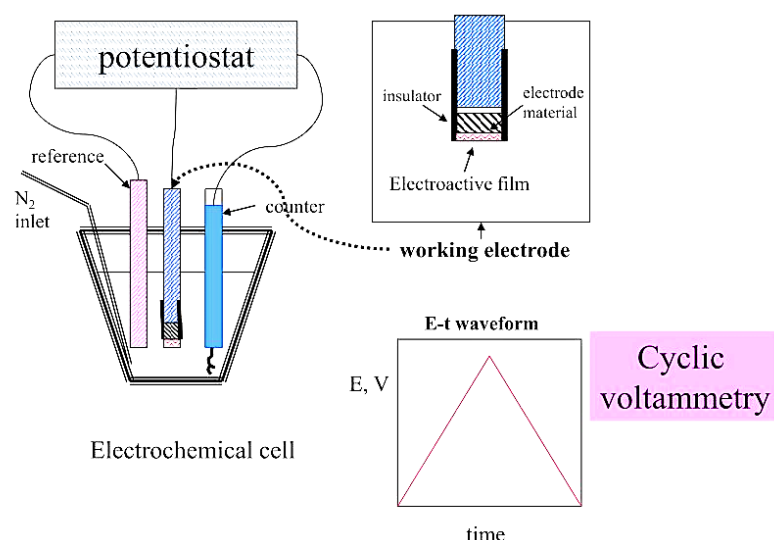


**Figure 9**: **A typical three-electrode system employed for electrochemical studies [reprinted from Parthasarathy, 86]**

We conducted Cyclic Voltammetry(CV) and Differential Pulse Voltammetry(DPV) to inspect the electrochemical properties of the electrodes with the help of a three-electrode system as shown in **Fig. 9**. For this purpose, we made use of a Phosphate

Buffer Solution (PBS, 50mM, 0.9% NaCl) consisting of 5mM of ferri-ferrocyanide redox couple ($Fe(CN)_6^{3-/4-}$). The choice of PBS solution may be attributed to its close resemblance to the ionic strength and atmosphere found in the biological species along with commendable compatibility with the biomolecules equipped with high electrode and pH stability [87]. We preferred the ferri-ferrocyanide redox couple for the electrochemical studies as it gives us an excellent one-electron redox reaction which is both simple and reversible making it best suited for studying the electrochemical properties of the electrodes [88]. In addition to this, the redox couple is so electro-active that it gives us very sharp and well-defined peaks in CV and DPV graphs which play a crucial role in calculating the precise values of currents and potentials in turn helping in the calibration and optimizing the experimental conditions [88].

### 3.2.1 Cyclic Voltammetry
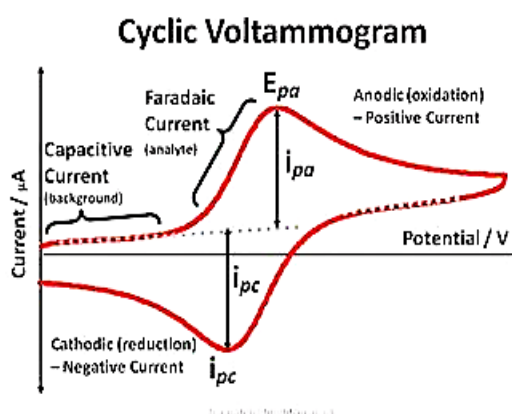


**Figure 10**: **Pictorial representation of the measurable physical parameters of Cyclic Voltammetry [reprinted from Khan et al., 92]**

Cyclic voltammetry (CV) is an essential technique used by researchers worldwide to gain insights into the kinetics and various parameters of electrochemical reactions at the electrode interface [89-91]. This method involves varying the applied potential and measuring the resulting current as a function of potential. In a three-electrode system, the potential is adjusted across the reference and working electrode, and the resulting current is measured between the counter and the working electrode. In cyclic voltammetry, a triangular potential is employed, with the potential being swept back and forth, hence the term "cyclic." The rate at which this potential is varied over time is known as the scan rate. By increasing the potential, we enhance the repulsion force

acting on the substrate's electrons, leading to the liberation of electrons once the potential exceeds the substrate's ionization potential, resulting in oxidation. Conversely, decreasing the potential leads to the reduction or acceptance of electrons. **Fig. 10** provides a visual representation of the mechanism behind the cyclic voltammetry test.

This means during the forward scan, when the change in the potential is positive we have the occurrence of oxidation and during the reverse scan we have the occurrence of reduction. The graph that is drawn between the potential swept and resulting current (scientifically known as voltamogram) communicates many important features about the process. One of them is the nature of the reaction. If the plot is in the form of a closed duck-shaped curve, then it implies that the reaction occurring in the vicinity of the electrodes is reversible. If the plot is closed and the shape has a notable deviation from that of the duck it implies that the process is quasi-neutral. This means that even though the system can come back to its initial state but may suffer from some energy loss. And if the plot is neither of them then the process is irreversible. All the possible curves that can retained during the potential sweep are depicted in **Fig. 11**.
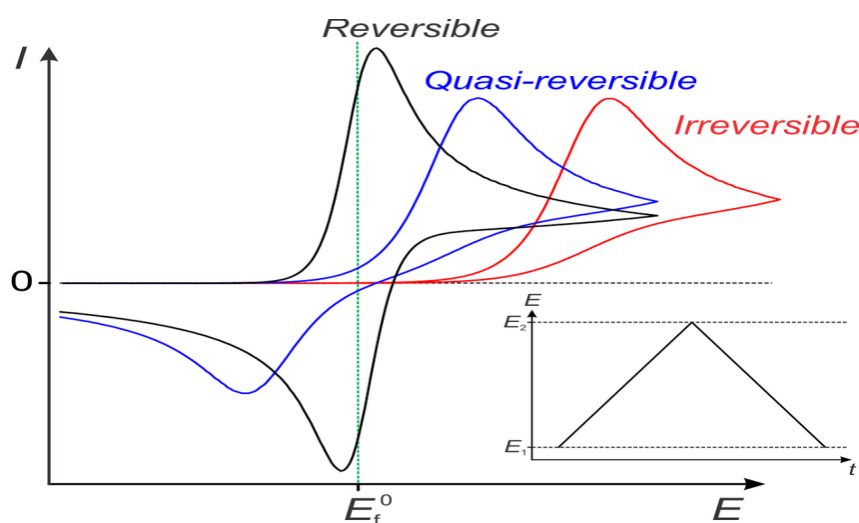


**Figure 11**: **Curves of Cyclic Voltammetry for the reversible, irreversible, and quasi-reversible process [reprinted from Lee et al., 93]**

Mathematically, if the difference between the cathodic and anodic peak potential (i.e., $\Delta E_p = E_{pc} - E_{pa}$) is less than 57 mV, then the process can be considered reversible [16]. Physically Nernst equation predicts the equilibrium potential that needs to be applied externally so that there is no movement of ions, that is the motion of the ions due to

diffusion which arises due to differences in concentration is countered by the motion of the ions due to external potential.

### 3.2.2 Differential Pulse Voltammetry (DPV)
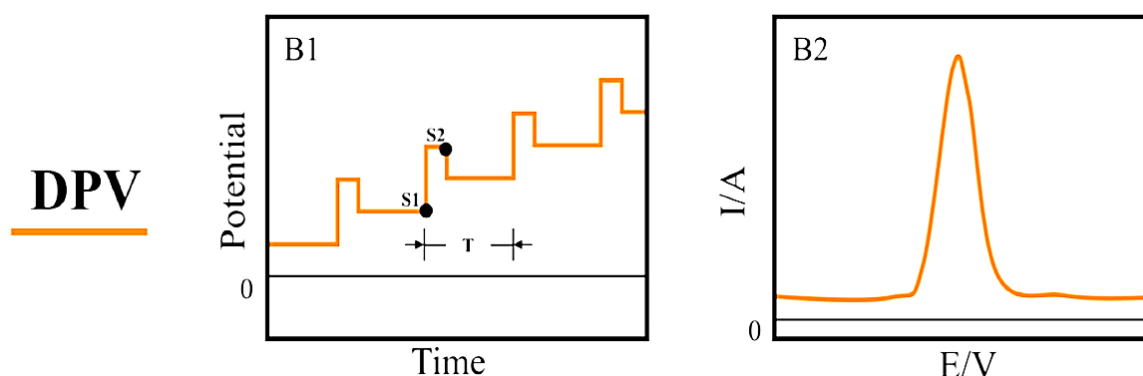


**Figure 12**: **Pictorial description of the applied voltage and response curve of Differential Pulse Voltammetry [reprinted from Liu et al., 94]**

It is a type of voltammetry technique, a potential scan is made by using a series of pulses with constant amplitude, superimposed on the dc-potential (also called linear ramp potential), consequently, the response of current is in the form of peaks as shown in **Fig. 12**. Hence by using a series of voltage pulses we measure the current response of electroactive species in a solution. It is instrumental in determining the oxidation and reduction process depending on the analyte concentration [95, 96].



**Figure 13**: **Linear Ramp Potential scan employed in a differential pulse Voltammetry [Source: Knowledge Base, Palmsens: online,95]**

23

In **Fig. 13**, it is clear that $I_1$ represents the electrochemical current measured before applying the pulse at time $t_1$ and $I_2$ represents the electrochemical current measured at the end of time $t_2$, then $\Delta I$ gives the peak-like response current and is given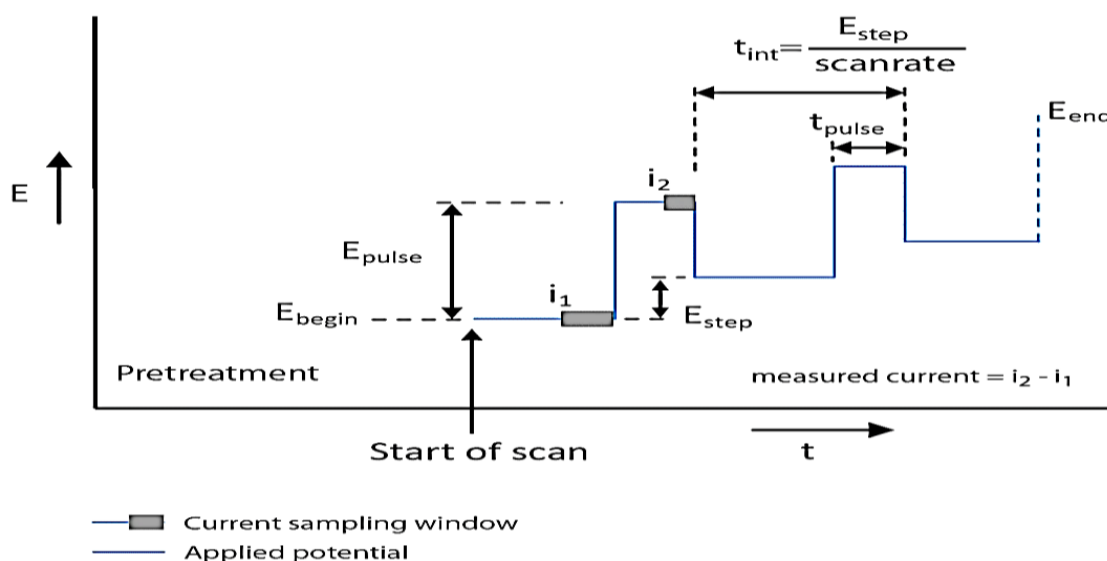 by $I_2-I_1$. And the highest peak is directly proportional to the concentration of the analyte [96]. The keynote advantages and disadvantages of this technique were found to be as follows [96, 97]:

**Advantages:**

1. **High Sensitivity**: DPV offers high sensitivity, making it suitable for the analysis of trace amounts of substances in solution. This is because it employs differential pulses which minimizes the background noise.

2. **Selective Detection**: By subtracting the baseline current, DPV can enhance selectivity by eliminating background noise and interference from other species in the solution.

3. **Low Background Current**: DPV typically exhibits low background current, which improves the signal-to-noise ratio and enhances the detection limit.

4. **Wide Range of Applications**: DPV is versatile and can be applied to various electrochemical systems, including the analysis of organic compounds, metal ions, and biomolecules

In summary, while DPV offers high sensitivity and selective detection, its implementation can be complex, requiring specialized equipment and careful optimization of experimental parameters. However, its versatility and ability to analyze trace substances make it a valuable tool in electrochemical research and analysis

# CHAPTER 4- RESULTS AND DISCUSSIONS

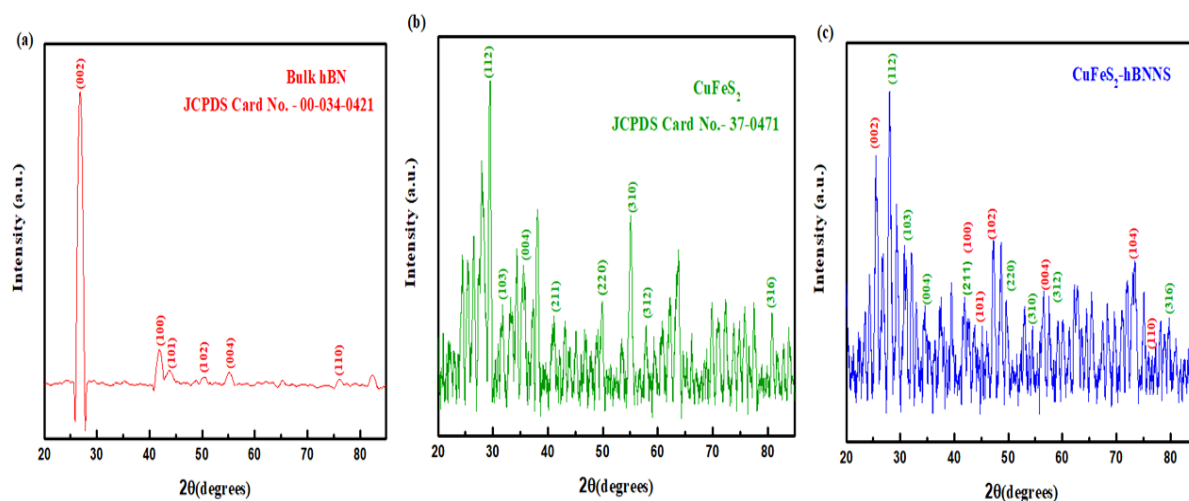## 4.1 MATERIAL CHARACTERIZATION

### 4.1.1 X-ray Diffraction



**Figure 14: X-ray diffraction of (a) Bulk h-BN, (b) CuFeS$_2$, and (c) CuFeS$_2$-hBNNS respectively.**

**Fig. 14** depicts the x-ray diffraction (XRD) results of the as-synthesized CuFeS$_2$ and CuFeS$_2$-hBNNS, carried out in the range 20 to 80°. The studies were carried out to comprehend the crystallinity and phase of the as-prepared products. **Fig. 14(a)** illustrates the XRD pattern of the Bulk h-BN portraying sharp peaks positioned at 26.65°, 41.56°, 43.86°, 50.1°, and 55° corresponding to hkl planes (002), (100), (101), (102), and (004) which is found to be in lines with JCPDS card number 00-034-0421 [60, 16]. The peaks observed in **Fig. 14(b)** at 2Θ= 29.48°, 31.76°, 35.54°, 41.12°, 49.88°, 55.12°, 57.86°, and 80° were catalogued to the characteristic hkl planes of CuFeS$_2$ positioned at (112), (103), (004), (211), (220), (310), (312) and (316), which respectively matched with that of the tetragonal chalcopyrite phase having the JCPDS card number 37-0471 [ 16, 98-101]. The highest intensity observed at 29.48° suggests that the fabricated chalcopyrite was more structured along (112) plane. The notable existence of a peak at 27.98° may be inferred from the presence of CuS particles [101]. Further, the XRD pattern of the nanocomposite demonstrated the presence of peaks of both the chalcopyrite and Bulk h-BN. The peaks at 25.48°, 41.92°, 43.66°,47.24°, 56.44°,73.44° and 76.04° were attributed to (002), (100), (101), (102), (004), (104) and (110) planes of the bulk h-BN, while those at 29.02°, 31°, 34.52°, 41.92°, 49.6°,

25

54.38°, 57.52° and 79.82° may be indexed to the planes given as (112), (103), (004), (211), (220), (310), (312) and (316) confirming the phase formation of the chalcopyrite in the nanocomposite

There is a keynote absence of the peak at 27.98° in the case of the nanocomposite, which indicates that the impure phase of CuS reacted to produce many more $CuFeS_2$ nanoparticles [101], thus concluding the fact that the fabricated nanocomposite turns out to be much purer than the earlier produced chalcopyrite. Hence, the high crystalline behavior demonstrated by the XRD pattern of the nanocomposite infers that $CuFeS_2$ has been successfully fostered on hBNNS.

## 4.1.2 Scanning Electron Microscopy (SEM)
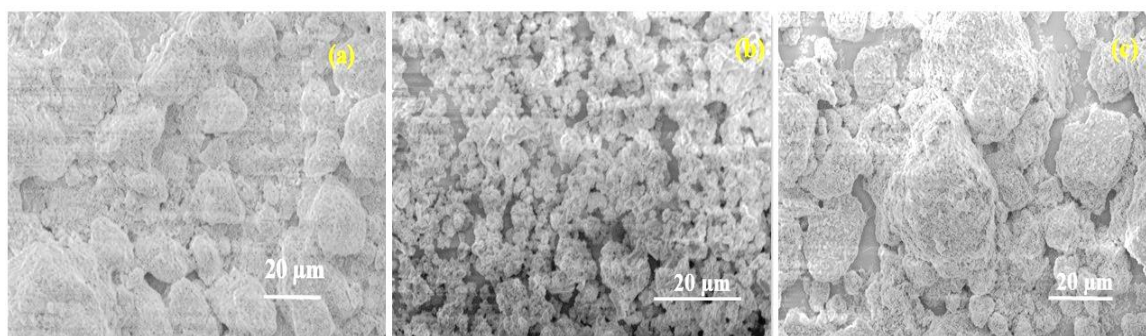


**Figure 15: Scanning Electron microscopy images of (a) Bulk h-BN, (b) CuFeS₂, and (c) CuFeS₂-hBNNS scanned at 20 μm respectively**

The morphological and structural characteristics of the as-synthesized chalcopyrite and nanocomposite were comprehensively examined using a scanning electron microscope (SEM). This analysis was instrumental in gaining insights into the surface morphology and topographical changes of each sample during the synthesis process. **Fig. 15(a)** provides a visual representation of the SEM analysis of Bulk h-BN at a scale of 20 μm, revealing the presence of Bulk h-BN in the form of large clusters. Furthermore, **Fig. 15(b)** illustrates the outcome of the suggested hydrothermal synthesis, showcasing two-dimensional $CuFeS_2$ nanoparticles arranged in the shape of a flower with smooth surfaces. Subsequently, **Fig. 15(c)** presents the SEM analysis of the nanocomposite at a 20 μm scale, indicating that the in-situ hydrothermal treatment facilitated the successful deposition of $CuFeS_2$ onto hBNNS, resulting in the formation of tiny nanoparticles of $CuFeS_2$ decorated on the surface of hBNNS.

## 4.1.3 Fourier Transform Infrared Spectroscopy (FT-IR)

The Fourier Transform Infrared Spectroscopy (FT-IR) analysis was performed within the range of 400 cm$^{-1}$ to 4000 cm$^{-1}$ to thoroughly examine the bond formation and functionalization in (i) Bulk h-BN, (ii) CuFeS$_2$, and (iii) CuFeS$_2$-hBNNS, as depicted in **Fig. 16**. The spectrum of CuFeS$_2$ unequivocally demonstrates a prominent peak at 619.02 cm$^{-1}$, directly linked to the distinctive interactions with the metals, signifying the stretching of the S-O bond [100]. Furthermore, the peaks at 482.95 cm$^{-1}$ and 732.48 cm$^{-1}$ unambiguously correspond to the vibrations of Fe-SO$_4$ [102], establishing the connection between the vibrations of copper sulfate species and those of ferrous sulfate species [100]. This unequivocally suggests the successful bonding between copper and sulfur. Similarly, the peaks at 1114.66 cm$^{-1}$, 1629.48 cm$^{-1}$, and 1401.50 cm$^{-1}$ are indisputably attributable to Cu-CO, Fe-C=O, and Fe-COO bond bending and stretching, respectively [103]. Finally, the peaks at 2856.42 cm$^{-1}$, 2921.91 cm$^{-1}$, and 3444.91 cm$^{-1}$ unambiguously signify OH bond stretching, as supported by references [100, 102, 103]
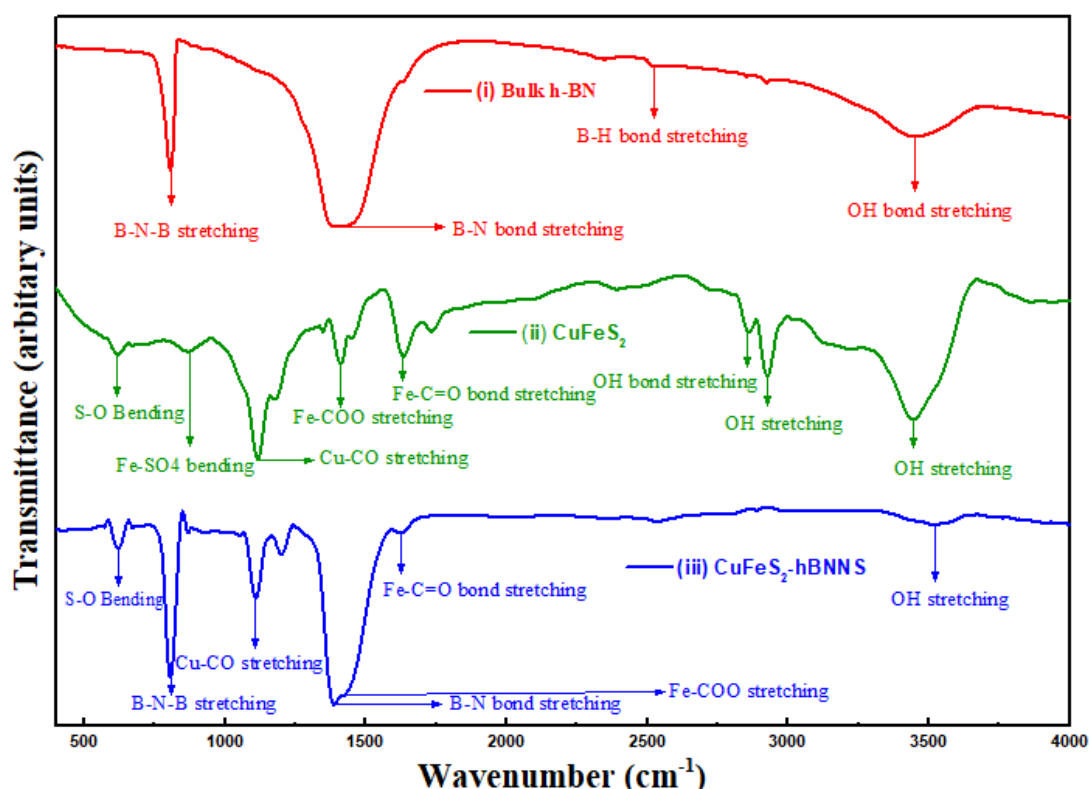


**Figure 16: FT-IR spectra of (i) Bulk h-BN, (ii) CuFeS$_2$, and (iii) CuFeS$_2$-hBNNS**

A bunch of peaks were observed on closely examining the FT-IR spectra of the developed nanocomposite (CuFeS$_2$-hBNNS). The presence of peaks in the fingerprint

region of the spectra corresponding to CuFeS$_2$ and h-BNNS confirms that the bond formation and functionalization of the materials have been successfully achieved through the prescribed one-pot hydrothermal synthesis route. The presence of B-N-B stretching, B-N bond stretching, and B-H bond stretching was validated by the peaks at 812 cm$^{-1}$, 1395 cm$^{-1}$, and 2510 cm$^{-1}$ respectively.

The trail of small indistinguishable peaks within the 3219 cm$^{-1}$ to 3519 cm$^{-1}$ range corresponds to N-H bond stretching [16, 60]. The characteristic peak depicting the S-O bond was perceived at 620 cm$^{-1}$. The peaks at 1106 and 1420 cm$^{-1}$ positively confirm the presence of Cu-CO, and Fe-COO bond stretches. While the peaks at 3447 cm$^{-1}$ and 1626 cm$^{-1}$ depict OH bond stretching and Fe-C=O bond stretches. Finally, the doublet peaks at 2797 cm$^{-1}$ and 2890 cm$^{-1}$ are the indicators of C-H bond stretching respectively [39-41]. The presence of peaks in the fingerprint region of the spectra corresponding to CuFeS$_2$ and h-BNNS confirms that the bond formation and functionalization of the materials have been successfully achieved through the prescribed one-pot hydrothermal synthesis route, and the findings of the FT-IR spectroscopy have been tabulated which confirms the bond formations at each step of synthesis.

**Table 1: FT-IR spectra results of Chalcopyrite (CuFeS$_2$)**

| S.No. | Wavenumber(cm$^{-1}$) | Assigned Peaks |
|---|---|---|
| 1. | 482.95 | Fe-SO$_4$ vibrations |
| 2. | 615.59 | S-O bond bending |
| 3. | 732.48 | Fe-SO$_4$ vibrations |
| 4. | 1114.66 | Cu-CO stretching mode |
| 5. | 1629.48 | Fe-C=O bond stretch |
| 6. | 1401.50 | Fe-COO stretching mode |
| 7. | 2856.42 | OH bond stretching |
| 8. | 2921.91 | OH stretching |
| 9. | 3444.91 | OH stretching |

**Table 2: FT-IR spectra results of Bulk h-BN**

| S.No. | Wavenumber (cm$^{-1}$) | Assigned Peaks |
|---|---|---|
| 1. | 812 | B-N-B stretching |
| 2. | 1395 | B-N bond stretching |
| 3. | 2510 | B-H bond stretching |
| 4. | 3219-3519 | N-H bond stretching |
| 5. | 3505 | OH bond stretching |

**Table 3: FT-IR spectra of the fabricated nanocomposite (CuFeS$_2$-hBNNS)**

| S.No. | Wavenumber(cm$^{-1}$) | Assigned Peak |
|---|---|---|
| 1. | 812 | B-N-B stretching |
| 2. | 1395 | B-N bond stretching |
| 3. | 2510 | B-H bond stretching |
| 4. | 3219-3519 | N-H bond stretching |
| 5. | 3505 | OH bond stretching |
| 6. | 620 | S-O bond |
| 7. | 1106 | Cu-CO stretches |
| 8. | 1420 | Fe-COO bond stretches |
| 9. | 1626 | Fe-C=O bond stretches |
| 10. | 2797 | C-H bond stretching |
| 11. | 2890 | C-H bond stretching |
| 12. | 3447 | OH bond stretching |

## 5.1.4 UV-Visible Spectroscopy Analysis
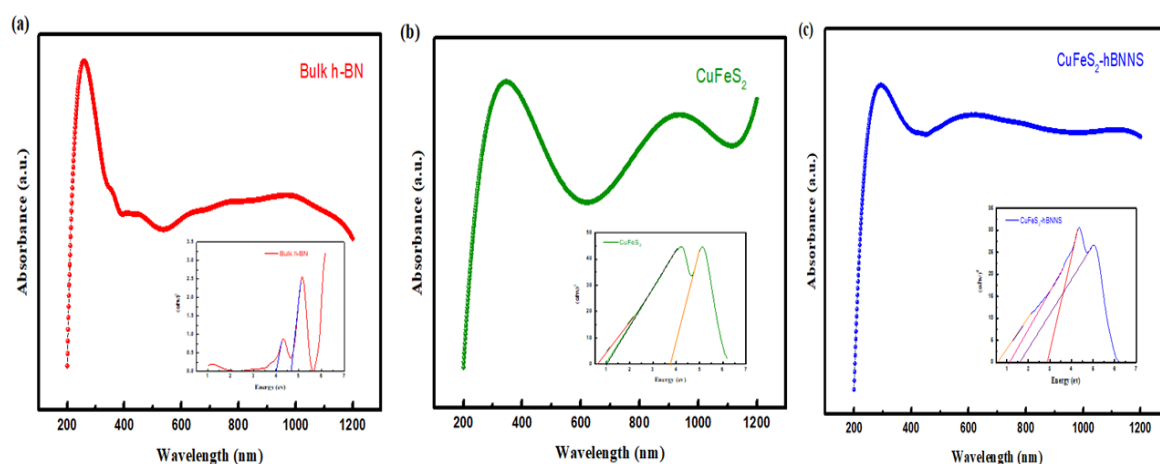


**Figure 17: UV-Vis spectra of (a) Bulk h-BN, (b) CuFeS₂, and (c) CuFeS₂-hBNNS respectively**.

The obtained visible and ultraviolet spectra of the synthesized chalcopyrite shown in **Fig. 17** were seen to exhibit two large peaks: one at 339 nm, exactly in the 300–400 nm range, and the other at 928 nm, exactly in the 900–1000 nm range. At 650 nm, a little peak was also seen. All the mentioned peaks were corroborated with the previous works [104]. As per the literature [102], it can be ascertained that the strong band at 339 nm is related to the distinct energy transition of the $Fe^{3+}$, specifically the transition corresponding to $^{6}A_1 \rightarrow {^4}E$ ($^4$D). However, the existence of $Fe^{3+}$ is once again confirmed by the peak at 928 nm, which was weaker than the prior one. Ultimately, a considerably weaker peak at 630 nm indicates that $Cu^{2+}$ is present in the sample [102]. The nanocomposite consists of notable peaks given by 300 and 600 nm resembling peaks of the CuFeS₂. All the wavelengths corresponding to the CuFeS₂ were also observed to be present in the UV-visible spectra of the nanocomposite.

The optical band gap of calculated from the Tauc plot associated with CuFeS₂ corresponds to 0.99 eV and 3.69 eV respectively by extrapolating the tangents to the x-axes. Based on the absorbance data, one may conjecture that the energy band determined at 0.99 eV, may potentially correlated to the wavelength transition of 928 nm, and another wavelength that could correspond to 339 nm. The band gap energies of Bulk h-BN were found to be between 4.69 and 3.83 eV based on the Tauc plot. Likewise, the nanocomposite's Tauc plot, which was projected to the x-axis, displays four large energy band gaps. The values were determined to be 2.91 eV, 1.74 eV, 0.68 eV, and 0.99 eV. In comparison, it is clear that the nanocomposite has the

contribution of chalcopyrite. It can also be noted that the optical band gap of h-BN was observed to be shifted after the nanocomposite formation owing to the reinforcement of $CuFeS_2$ in the nanocomposite. Hence from the UV-visible absorbance spectroscopy and Tauc plot, it can be concluded that hBNNS has undergone band-gap tuning and the number of optical states have significantly changed when hBNNS and $CuFeS_2$ are combined.

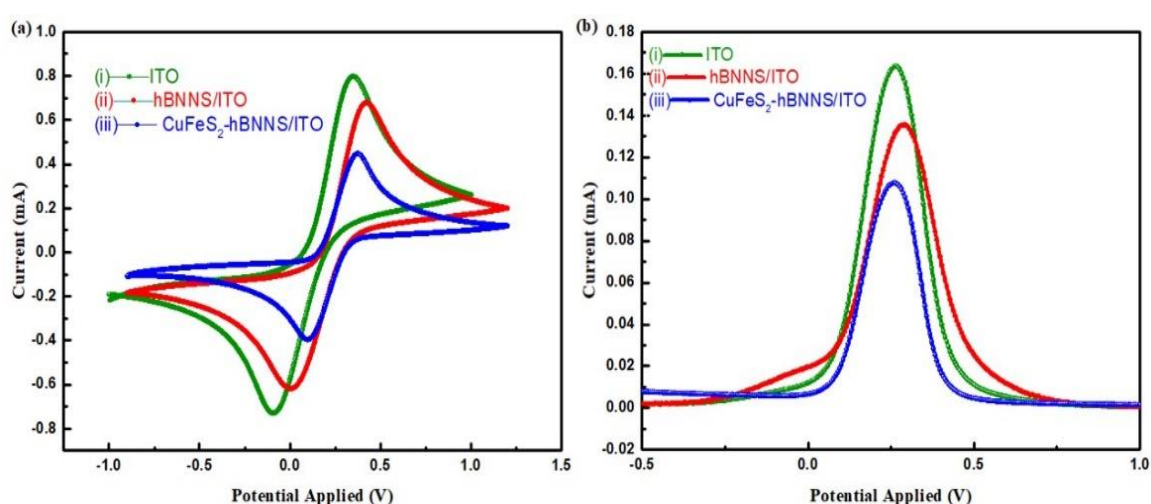## 4.2 Electrochemical Studies

## 4.2.1 Electrode Studies



**Figure 18**: **Electrode study of (i) ITO, (ii) hBNNS/ITO, (iii) CuFeS₂-hBNNS/ITO performed using (a) CV, (b) DPV scanned at 50 mV/s respectively**.

Based on **Fig. 18**, the peak currents for the ITO slides during the CV and DPV analysis were noted to be 0.798 mA and 0.1637 mA, respectively. However, after modifying the electrode with hBNNS and chalcopyrite, there was a limited decline in both values. During the CV and DPV studies conducted on the h-BNNS/ITO electrode, the peak currents were observed to be 0.6787 mA and 0.1355 mA. In the case of $CuFeS_2$-hBNNS/ITO, its values were noted to decrease to 0.4477 mA and 0.1078 mA in the case of CV and DPV analysis. Thus, the reinforcement of $CuFeS_2$ on hBNNS in the nanocomposite resulted in a decrement in the diffusion rate, signifying a significant decrease in electron diffusion. The nanocomposite hindered the facile electron transfer process occurring between the electrode and PBS due to its large electroactive surface. This can also be inferred from the drastic decrement of the area under the respective curves. The area under the curve can infer the number of charges involved in the

31

reactions, which again proves the point that the amount of charges that are mobile or involved in the reactions drastically decreases when the ITO slide was modified with the hBNNS and further by the $CuFeS_2$.

One of the observations from the graphs describing the cyclic voltammetry curves of hBNNS/ITO and $CuFeS_2$-hBNNS/ITO is that by carefully zooming on the x-axis at the point when the current gradually increases during the oxidation cycles, the potential at which the currents gains a non-zero value which is known as oxidation potential was found to be smaller for the chalcopyrite electrode than that of the hBNNS. The importance of the oxidation potential is that it depicts the minimum potential that needs to be applied so that the electrode becomes electrically active. The oxidation potential for hBNNS/ITO was 0.17 V and that of $CuFeS_2$-hBNNS/ITO was 0.13 V. This can be treated as evidence for chalcopyrite enhancing the chemical and electrical properties of hBNNS.

**Table 4: Diffusion coefficients calculated using the Randle -Sevcik equation for each modification of the electrode**

| Modifications in the electrode | Anodic Peak Current (mA) | Diffusion Coefficients ($cm^2/s$) |
|---|---|---|
| **ITO** | **0.7980** | **0.704 X $10^{-11}$** |
| **hBNNS/ITO** | **0.6787** | **0.509 X $10^{-11}$** |
| **$CuFeS_2$-hBNNS/ITO** | **0.4477** | **0.22 X $10^{-11}$** |

After careful calculations of the magnitude of the peak currents for each step of modification of the electrodes from the cyclic voltammetry, with the help of the Randle- Sevcik equation [102], mathematically expressed as follows:

$$I_p = \left(2.69 \ X \ 10^5\right)ACD^{\frac{1}{2}}\sqrt{v}n^{\frac{3}{2}} \tag{4}$$

**Wherein, $I_p$ denotes the anodic peak current of the modified electrode**

**A represents the effective electroactive surface area of the electrode (1 $cm^2$)**

**C is the concentration of the redox species (5 X $10^{-3}$ M)**

**D is the diffusion coefficient**

**n represents the number of electrons that are transferred during the redox reaction (n=1)**

**ν is the scan rate (50mV/s)**

The diffusion coefficients were successfully calculated, and the following table summarizes the findings:

The calculated diffusion coefficients for each of the modifications of the working electrode have displayed a decreasing trend. Thus the reduced values of the diffusion coefficient confirm that each step of modification of the ITO slide drastically affected the kinetics of the electrode and obstructed the electron transfer between the slide and the redox couple. The decreasing trend in diffusion coefficients for each modification of the working electrode clearly indicates the significant impact of the ITO slide modifications on electrode kinetics. These reduced diffusion coefficients confirm the obstruction of electron transfer between the slide and the redox couple at each stage of modification.
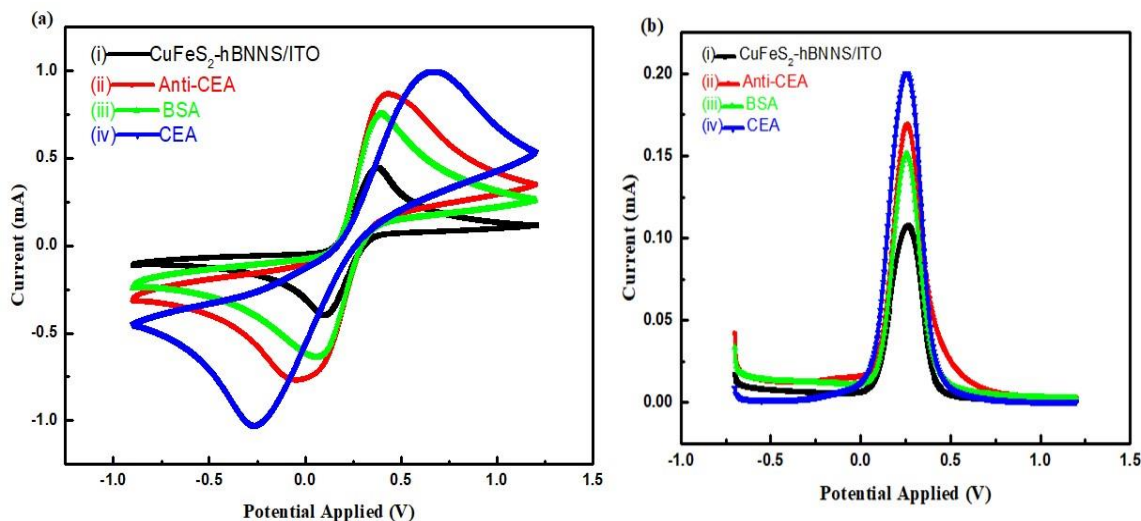
## 4.2.2 Electrode Modification Studies



**Figure 19**: **Protein immobilization onto CuFeS$_2$-hBNNS/ITO immunoelectrode monitored using (a) CV, and (b) DPV respectively scanned at 50 mV/s**.

After modifying the electrode with Anti-CEA, a remarkable increase in the peak current was observed, as illustrated in **Fig. 19**. The peak currents for the CV and DPV studies were 0.8657 mA and 0.1692 mA, representing a significant 90% increase from the previous levels. This substantial rise in current is attributed to the successful

33

immobilization of Anti-CEA on CuFeS$_2$-hBNNS/ITO, which promotes interactions facilitating enhanced electron transfer between the electrode and PBS solution. Moreover, the subsequent treatment of the electrode with BSA serves the dual purpose of preventing non-specific contributions from Anti-CEA and establishing precise interactions between antigen and antibody complexes. The noticeable decrease in peak current in the DPV and CV curves following the BSA treatment (0.1512 mA and 0.7516 mA, as depicted in **Fig. 19**) can be attributed to the obstructive nature of BSA, inhibiting electron transfer from disoriented Anti-CEA. Finally, the immobilization of CEA (Concentration- 1 ng/ml) resulted in record high peak currents in the CV and DPV plots (0.9967 mA and 0.2 mA, respectively), highlighting the successful cross-linking of CEA with Anti-CEA.

**Table 5: Diffusion coefficients calculated using the Randle -Sevcik equation after each protein immobilisation on the electrode**

| Modifications in the electrode | Anodic Peak Current (mA) | Diffusion Coefficients (cm$^2$/s) |
|---|---|---|
| Anti-CEA/CuFeS$_2$-hBNNS/ITO | 0.8657 | 0.829 X 10$^{-11}$ |
| BSA/Anti-CEA/CuFeS$_2$-hBNNS/ITO | 0.7516 | 0.620 X 10$^{-11}$ |
| CEA/BSA/Anti-CEA/CuFeS$_2$hBNNS/ITO | 0.9967 | 1.01 X 10$^{-11}$ |

The significant changes in the diffusion coefficients following the immobilization of BSA, Anti-CEA, and CEA at the working electrode surface strongly indicate successful binding. The changes in the diffusion coefficients indicates the rate of charge transfer or the redox species between the electrode and the PBS solution, which were obtained from CV studies with each modification. It quantifies the swift or slow movement of the redox species that diffuse towards the electrode, such that faster mass transport is characterised by higher values of diffusion coefficients. Notably, the highest diffusion coefficient observed for CEA immobilization can be attributed to the highly effective binding of CEA with Anti-CEA, resulting in

conformational changes within the protein and enhanced charge transfer, ultimately leading to an increased peak current.
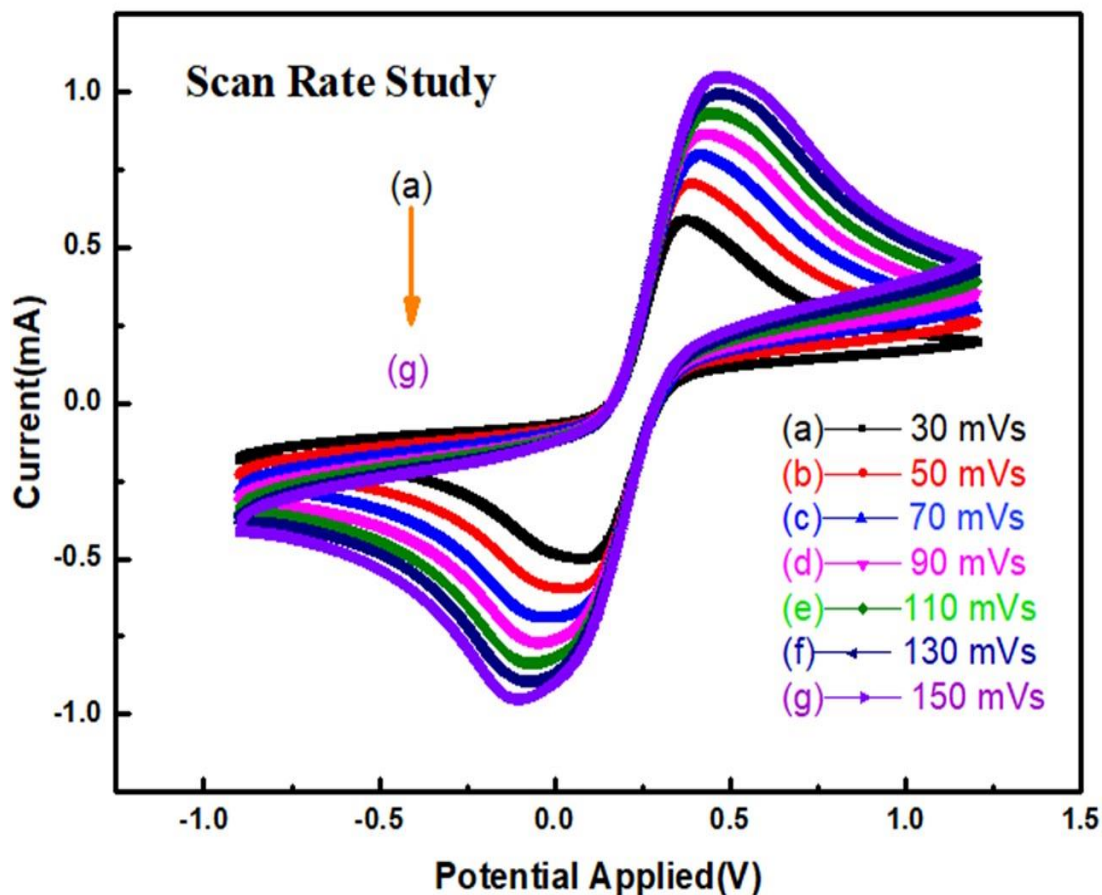
## 4.2.3 Scan Rate Studies



**Figure 20**: **The scan rate studies employed on the functionalized electrode BSA/Anti-CEA/CuFeS$_2$-hBNNS/ITO**

Furthermore, we conducted scan rate studies on the functionalized electrode, and the results are quite remarkable. Through cyclic voltammetry studies, we inspected the effect of scan rate on the stability of the immunoelectrode BSA/Anti-CEA/CuFeS$_2$-hBNNS/ITO, and the findings have been visually represented in **Fig. 20**. **Table 6** presents the observed peak anodic and cathodic currents for each scan rate. We then calculated the ratio of the currents, which is crucial in determining the nature of the process near the electrodes. According to the literature [105], when the ratio of peak currents for each scan rate is nearly equal to 1, it can be concluded that the process near the electrode's surface was quasi-reversible. Hence we can safely deduce that the nature of the process occurring at the surface of the fabricated electrode is quasi-

35

reversible. Upon detailed examination, it is evident that as we move towards higher scan rates, the ratio tends to approach 1. Thus, it can be inferred that at high scan rates, the nature of the process gradually shifts from quasi-reversible to reversible [105].

**Table 6: Tabular presentation of the peak anodic current ($I_{pa}$), peak cathodic current ($I_{pc}$), and ratio of $I_{pa}/I_{pc}$ for the functionalized electrode BSA/Anti-CEA/CuFeS$_2$-hBNNS/ITO**

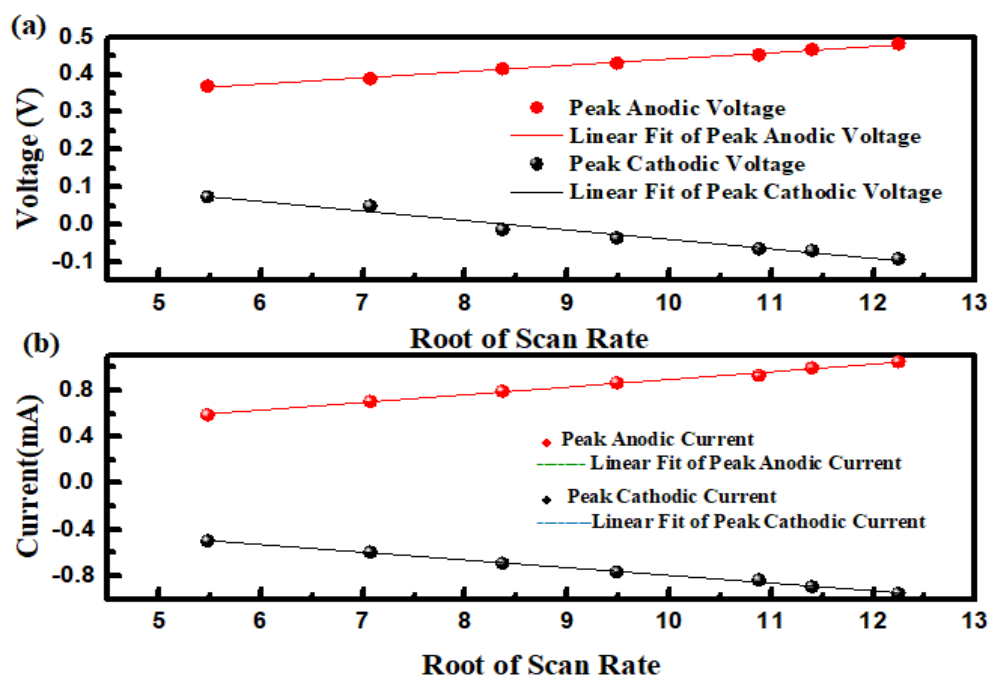| Scan Rate (mV/s) | Anodic Peak Current ($I_{pa}$)(mA) | Cathodic Peak Current ($I_{pc}$)(mA) | $I_{pa}/I_{pc}$ |
|---|---|---|---|
| 30 | 0.5901 | 0.4976 | 1.186 |
| 50 | 0.7046 | 0.5962 | 1.181 |
| 70 | 0.7937 | 0.6924 | 1.146 |
| 90 | 0.8658 | 0.7663 | 1.129 |
| 110 | 0.9305 | 0.8362 | 1.112 |
| 130 | 0.9927 | 0.8954 | 1.108 |
| 150 | 1.0468 | 0.9512 | 1.100 |



**Figure 21: (a) Peak anodic voltage and Cathodic voltage (b) Peak anodic and cathodic current linear variations with the root of scan rate (mV/s)**

36

**Fig**. **21** depicts the linearity relationship that the root of the scan with the respective cathodic and anodic current. The equations of the line were found to be in good agreement with the equation of a straight line given by y=mx+c, wherein m is the slope of the line, and c is the y-intercept. The equations of the observed straight lines are as follows:

$$I_a=0.066 \text{ [A}\sqrt{s}/mV] * \sqrt{v} \text{ [}\sqrt{mV/s}] + 0.234 \text{ [mA] } (R^2 = 0.996)$$

$$I_c=-0.066 \text{ [A}\sqrt{s}/mV] * \sqrt{v} \text{ [}\sqrt{mV/s}] + 0.131 \text{ [mA] } (R^2 = 0.997)$$

$$V_a=0.017 \text{ [V}\sqrt{s}/mV] * \sqrt{v} \text{ [}\sqrt{mV/s}] + 0.275 \text{ [mV] } (R^2 = 0.997)$$

$$V_c=-0.0252 \text{ [V}\sqrt{s}/mV] * \sqrt{v} \text{ [}\sqrt{mV/s}] + 0.213 \text{ [mV] } (R^2 = 0.974)$$

Wherein, $I_a$ is the anodic current, $I_c$ is the cathodic current, $V_a$ is the anodic voltage, $V_c$ is the cathodic voltage, and $v$ is the scan rate. The importance of this linear behavior is that it claims that the process occurring at the electrodes is diffusion-controlled in nature. This means that there is no intrinsic contribution towards the sensing. This depicts that the proposed nanocomposite displays immense potential for biosensing applications with accurate and reliable sensing capabilities.

# CONCLUSIONS AND FUTURE SCOPE OF WORK

This investigation meticulously explored the potential of $CuFeS_2$-hBNNS nanocomposite for applications in biosensing. The nanocomposite was synthesized using a rigorously controlled one-pot hydrothermal method, ensuring high purity without any harmful residues. XRD analysis conducted across a comprehensive range of 20° to 80° confirmed the successful formation of the desired phase formation and the exceptional purity of the as-fabricated nanocomposite. SEM provided a high-resolution visualization of the morphology and surface characteristics of the nanocomposite at 20 scale. The micrographs convincingly demonstrated the successful anchoring of chalcopyrite nanoparticles onto individual hBNNS, resulting in a unique architecture of nanoparticles decoration on two-dimensional nanosheets. Further characterization through FT-IR provided compelling evidence for the formation of bonds at each stage of the synthesis process. This analysis confirmed the successful bonding between constituent atoms and the functionalization of the nanocomposite. Evaluation of the optical properties of the $CuFeS_2$-hBNNS nanocomposite using UV-visible spectroscopy revealed distinct features, indicating an advantageous tuning of the band gap, that resulted in lowering the band gap associated with wide band gap of h-BN. Subsequent CV and DPV studies emphatically demonstrated the capability of the nanocomposite to provide stable binding sites for anchoring biomolecules. The successful cross-linking between proteins further underscored the immense potential of this nanocomposite for biosensing. Notably, the nanocomposite exhibited enhanced electroactivity compared to hBNNS alone, effectively overcoming the limitations imposed by the low catalytic properties of hBNNS. Moreover, scan rate studies showcased the nanocomposite's ability to maintain its exceptional characteristics even across a broad range of scan rates. This observation signifies the nanocomposite's sensitivity and durability, making it a highly desirable material for biosensing applications. Furthermore, the observed linearity between the cathodic and anodic voltages and currents with the square root of scan rates provided strong evidence for a diffusion-controlled process occurring near the fabricated electrode. In conclusion, this study successfully identified a promising candidate material exhibiting several key advantages, including cost-effectiveness, excellent reproducibility, minimal toxicity, biodegradability for the development of next-generation, point-of-care diagnostic devices.

# REFERENCES

[1.] Wibowo, Yudha Gusti, Bimastyaji Surya Ramadan, Tarmizi Taher, and Khairurrijal Khairurrijal. "Advancements of nanotechnology and nanomaterials in environmental and human protection for combatting the covid-19 during and post-pandemic era: a comprehensive scientific review." *Biomedical Materials & Devices* 2, no. 1 (2024): 34-57.

[2.] Zhang, Hua, Xiao Huang, and Ye Chen. "Introduction: Phase Engineering of Nanomaterials." *Chemical Reviews* 124, no. 2 (2024): 245-247.

[3.] Bell, Alexis T. "The impact of nanoscience on heterogeneous catalysis." *Science* 299, no. 5613 (2003): 1688-1691.

[4.] Daniel, Marie-Christine, and Didier Astruc. "Gold nanoparticles: assembly, supramolecular chemistry, quantum-size-related properties, and applications toward biology, catalysis, and nanotechnology." *Chemical reviews* 104, no. 1 (2004): 293-346.

[5.] Baughman, Ray H., Anvar A. Zakhidov, and Walt A. De Heer. "Carbon nanotubes--the route toward applications." *science* 297, no. 5582 (2002): 787-792.

[6.] Geim, Andre K., and Konstantin S. Novoselov. "The rise of graphene." *Nature materials* 6, no. 3 (2007): 183-191.

[7.] Alivisatos, A. Paul. "Semiconductor clusters, nanocrystals, and quantum dots." *science* 271, no. 5251 (1996): 933-937.

[8.] Maier, Stefan A. *Plasmonics: fundamentals and applications*. Vol. 1. New York: springer, 2007.

[9.] Peer, Dan, Jeffrey M. Karp, Seungpyo Hong, Omid C. Farokhzad, Rimona Margalit, and Robert Langer. "Nanocarriers as an emerging platform for cancer therapy." *Nano-enabled medical applications* (2020): 61-91.

[10.] Gupta, Ajay Kumar, and Mona Gupta. "Synthesis and surface engineering of iron oxide nanoparticles for biomedical applications." *biomaterials* 26, no. 18 (2005): 3995-4021.

[11.] **Two-Dimensional Nanomaterials** Zahra Rafiei-Sarmazdeh, Seyed Morteza Zahedi-Dizaji and Aniseh Kafi Kang https://doi.org/10.5772/intechopen.85263

[12.] Czepa, Włodzimierz, Dawid Pakulski, Alessandro Aliprandi, Artur Ciesielski, and Paolo Samorì. "Chemical sensing with 2D materials." *Chemical Society reviews* 47, no. 13 (2018).

[13.] **2D Nanomaterials** https://doi.org/10.3390/coatings10090897

[14.] Rizwan, M., Aleena Shoukat, Asma Ayub, Bakhtawar Razzaq, and Muhammad Bilal Tahir. "Types and classification of nanomaterials." In *Nanomaterials: synthesis, characterization, hazards and safety*, pp. 31-54. Elsevier, 2021.

[15.] Saleh, Tawfik A. "Nanomaterials: Classification, properties, and environmental toxicities." *Environmental Technology & Innovation* 20 (2020): 101067.

[16.] Kanika Sharma, Nitin K Puri, and Bharti Singh. An efficient electrochemical nano-biosensor based on hydrothermally engineered ultrathin nanostructures of hexagonal boron nitride nanosheets for label-free detection of carcinoembryonic antigen. Applied Nanoscience, pages 1–14, 2023.

[17.] Kanika Sharma and Nitin K Puri. Enhanced electrochemical performance of hydrothermally exfoliated hexagonal boron nitride nanosheets for applications in electrochemistry. Journal of The Electrochemical Society, 168(5):056512, 2021

[18.] Naclerio, Andrew E., and Piran R. Kidambi. "A review of scalable hexagonal boron nitride (h-BN) synthesis for present and future applications." *Advanced Materials* 35, no. 6 (2023): 2207374.

[19.] Liu, Lei, Y. P. Feng, and Z. X. Shen. "Structural and electronic properties of h-BN." *Physical Review B* 68, no. 10 (2003): 104102.

[20.] Emerging 2D Nanomaterials for Biomedical Applications https://doi.org/10.1016%2Fj.mattod.2021.04.020

[21.] 2D nanomaterials: beyond graphene and transition metal dichalcogenides https://doi.org/10.1039/C8CS90084A

[22.] Werner, T. T., Gavin Mark Mudd, and Simon Martin Jowitt. "Indium: key issues in assessing mineral resources and long-term supply from recycling." *Applied Earth Science* 124, no. 4 (2015): 213-226.

[23.] Ennaoui, A. et al. "CuInS2 Thin Film Solar Cells from a Molecular Precursor Solution and Their Photovoltaic Properties." Thin Solid Films, 1998

[24.] Mubeen, S. et al. "Heterogeneous Photocatalysis with Copper Aluminum Sulfide." Journal of Physical Chemistry C, 2014**.**

[25.] Tao, J. et al. "Solution-based synthesis and photovoltaic applications of CuAlS2 and CuAlSe2 nanocrystals." Journal of Materials Chemistry A, 2014

[26.] AC Lokhande, S Teotia, AR Shelke, T Hussain, IA Qattan, VC Lokhande, Shashikant Patole, JH Kim, and CD Lokhande. Chalcopyrite based carbon composite electrodes for high performance symmetric supercapacitor. Chemical Engineering Journal, 399:125711, 2020

[27.] Bhoomi S Shah, Jolly B Raval, Deepak Kumar, Sunil H Chaki, and MP Deshpande. A review on ternary cufes2 compound: Fabrication strategies and applications. Journal of Alloys and Compounds, page 168566, 2022

[28.] Suryavanshi, A. P., et al. "Nanocomposites: Properties and Applications." Journal of Composite Materials, 2021

[29.] Bogue, Robert. "Nanocomposites: a review of technology and applications." *Assembly Automation* 31, no. 2 (2011): 106-112.

[30.] Sonawane, Gunvant H., Sandip P. Patil, and Shirish H. Sonawane. "Nanocomposites and its applications." In *Applications of nanomaterials*, pp. 1-22. Woodhead Publishing, 2018.

[31.] Duarah, Rituparna, Deepshikha Hazarika, Aditi Saikia, Rajarshi Bayan, Tuhin Ghosh, and Niranjan Karak. "Sustainable Polymeric Nanocomposites for Multifaceted Advanced Applications." *Advances in Sustainable Polymers: Processing and Applications* (2019): 363-395.

[32.] Kim, S. H., et al. "Nanocomposites in Electronics." IEEE Transactions on Nanotechnology, 2020.

[33.] Gaharwar, Akhilesh K., Nicholas A. Peppas, and Ali Khademhosseini. "Nanocomposite hydrogels for biomedical applications." *Biotechnology and bioengineering* 111, no. 3 (2014): 441-453.

[34.] Shrivastava, Swati, Nimisha Jadon, and Rajeev Jain. "Next-generation polymer nanocomposite-based electrochemical sensors and biosensors: A review." *TrAC Trends in Analytical Chemistry* 82 (2016): 55-67.

[35.] Palanisamy, Periasamy, Murthy Chavali, Enamala Manoj Kumar, and Krishna Chitanya Etika. "Hybrid nanocomposites and their potential applications in the field of nanosensors/gas and biosensors." In *Nanofabrication for Smart Nanosensor Applications*, pp. 253-280. Elsevier, 2020.

[36.]Bychkov A. WHO classification. PathologyOutlines.com website. https://www.pathologyoutlines.com/topic/lungtumorWHO.html. Accessed February 11th, 2024

[37.] Seigel, R., and A. Jemal. "American Cancer Society: Cancer Facts and Figures 2015." *American Cancer Society: Atlanta, GA, USA* (2015).

[38.] Thun, Michael J., Lindsay M. Hannan, Lucile L. Adams-Campbell, Paolo Boffetta, Julie E. Buring, Diane Feskanich, W. Dana Flanders et al. "Lung cancer occurrence in never-smokers: an analysis of 13 cohorts and 22 cancer registry studies." *PLoS medicine* 5, no. 9 (2008): e185

[39.] Krewski, Daniel, Jay H. Lubin, Jan M. Zielinski, Michael Alavanja, Vanessa S. Catalan, R. William Field, Judith B. Klotz et al. "Residential radon and risk of lung cancer: a combined analysis of 7 North American case-control studies." *Epidemiology* (2005): 137-145.

[40.] Darby, Sarah, D. Hill, A. Auvinen, J. M. Barros-Dios, H. Baysson, F. Bochicchio, H. Deo et al. "Radon in homes and risk of lung cancer: collaborative analysis of individual data from 13 European case-control studies." *Bmj* 330, no. 7485 (2005): 223

[41.] O'Reilly, KATHERINE MA, Anne Marie Mclaughlin, William S. Beckett, and Patricia J. Sime. "Asbestos-related lung disease." *American family physician* 75, no. 5 (2007): 683-688

[42.] Vineis, Paolo, and Kirsti Husgafvel-Pursiainen. "Air pollution and cancer: biomarker studies in human populations." *Carcinogenesis* 26, no. 11 (2005): 1846-1855

[43.] Pope Iii, C. Arden, Richard T. Burnett, Michael J. Thun, Eugenia E. Calle, Daniel Krewski, Kazuhiko Ito, and George D. Thurston. "Lung cancer, cardiopulmonary mortality, and long-term exposure to fine particulate air pollution." *Jama* 287, no. 9 (2002): 1132-114

[44.] King, Richard A., Jerome I. Rotter, and Arno G. Motulsky, eds. *The genetic basis of common diseases*. Oxford university press, 2002

[45.] Kasper, Dennis, Anthony Fauci, Stephen Hauser, Dan Longo, J. Jameson, and Joseph Loscalzo. *Harrison's principles of internal medicine, 19e*. Vol. 1, no. 2. New York, NY, USA:: Mcgraw-hill, 2015.

[46.] Holland, James F. *Holland-Frei cancer medicine 8*. Vol. 8. PMPH-USA, 2010

[47.] Byrd, David R., Robert K. Brookland, Mary Kay Washington, Jeffrey E. Gershenwald, Carolyn C. Compton, Kenneth R. Hess, Daniel C. Sullivan, and J. Milburn Jessup. *AJCC cancer staging manual*. Edited by Mahul B. Amin, Stephen B. Edge, and Frederick L. Greene. Vol. 1024. New York: springer, 2017.

[48.] Sharma, Kanika, Nitin K. Puri, and Bharti Singh. "An efficient electrochemical nano-biosensor based on hydrothermally engineered ultrathin nanostructures of hexagonal boron nitride nanosheets for label-free detection of carcinoembryonic antigen." *Applied Nanoscience* (2023): 1-14

[49.] Okada, Morihito, Wataru Nishio, Toshihiko Sakamoto, Kazuya Uchino, Tsuyoshi Yuki, Akio Nakagawa, and Noriaki Tsubota. "Prognostic significance of perioperative serum carcinoembryonic antigen in non-small cell lung cancer: analysis of 1,000 consecutive resections for clinical stage I disease." *The Annals of Thoracic Surgery* 78, no. 1 (2004): 216-221

[50.] Lee, Dong Soo, Seung Joon Kim, Jin Hyoung Kang, Sook Hee Hong, Eun Kyoung Jeon, Young Kyoon Kim, Ie Ryoung Yoo et al. "Serum carcinoembryonic antigen levels and the risk of whole-body metastatic potential in advanced non-small cell lung cancer." *Journal of Cancer* 5, no. 8 (2014): 663

[51.] A. Navrotsky, "Hydrothermal Synthesis of Nanomaterials," Journal of Materials Chemistry, vol. 19, no. 45, pp. 7521-7529, 2009

[52.] Darr, Jawwad A., Jingyi Zhang, Neel M. Makwana, and Xiaole Weng. "Continuous hydrothermal synthesis of inorganic nanoparticles: applications and future directions." *Chemical reviews* 117, no. 17 (2017): 11125-11238.

[53.] Shandilya, M., R. Rai, and J. Singh. "Hydrothermal technology for smart materials." *Advances in Applied Ceramics* 115, no. 6 (2016): 354-376.

[54.] S. Liu, R. Jin, and C. Chen, "Hydrothermal Synthesis of Metal Oxide Nanostructures for Catalytic Applications," Catalysis Today, vol. 174, no. 1, pp. 169-174, 2011.

[55.] Rabenau, Albrecht. "The role of hydrothermal synthesis in preparative chemistry." *Angewandte Chemie International Edition in English* 24, no. 12 (1985): 1026-1040.

[56.] He, Wenzhi, Guangming Li, Lingzhao Kong, Hua Wang, Juwen Huang, and Jingcheng Xu. "Application of hydrothermal reaction in resource recovery of organic wastes." *Resources, Conservation and Recycling* 52, no. 5 (2008): 691-699.

[57.] Darr, Jawwad A., Jingyi Zhang, Neel M. Makwana, and Xiaole Weng. "Continuous hydrothermal synthesis of inorganic nanoparticles: applications and future directions." *Chemical reviews* 117, no. 17 (2017): 11125-11238.

[58.] Riman, Richard E., Wojciech L. Suchanek, and Malgorzata M. Lencka. "Hydrothermal crystallization of ceramics." In *Annales de Chimie Science des Materiaux*, vol. 27, no. 6, pp. 15-36. No longer published by Elsevier, 2002.

[59.] Surjit Sahoo, Parthiban Pazhamalai, Vimal Kumar Mariappan,Ganesh Kumar Veerasubramani, Nam-Jin Kim, and Sang-Jae Kim. Hy- drothermally synthesized chalcopyrite platelets as an electrode material for symmetric supercapacitors. *Inorganic Chemistry Frontiers*, 7(7):1492– 1502, 2020

[60.] Kanika Sharma, Nitin K Puri, and Bharti Singh. An efficient electrochem-ical nano-biosensor based on hydrothermally engineered ultrathin nanos- tructures of hexagonal boron nitride nanosheets for label-free detection of carcinoembryonic antigen. *Applied Nanoscience*, pages 1–14, 2023

[61.] Aydın, Elif Burcu, and Mustafa Kemal Sezgintürk. "Indium tin oxide (ITO): A promising material in biosensing technology." *TrAC Trends in Analytical Chemistry* 97 (2017): 309-315

[62.] A. B. Fischer and K. H. Schwartzkopf, "Effects of Water Quality on Surface Chemistry of ITO Films," Journal of Applied Surface Science, vol. 255, no. 12, pp. 6211-6217, 2009

[63.] M. A. A. Schoenitz and J. M. Drelich, "Influence of Water Purity on Surface Hydrolysis of Metal Oxides," Langmuir, vol. 23, no. 10, pp. 5726-5730, 2007

[64.] E. T. Vandenberg and T. A. Golovchenko, "Improving Biosensor Sensitivity Using Deionized Water," Sensors and Actuators B: Chemical, vol. 180, pp. 587-594, 2013

[65.] Pundir, Chandra S., Ritu Deswal, and Vinay Narwal. "Quantitative analysis of hydrogen peroxide with special emphasis on biosensors." *Bioprocess and biosystems engineering* 41, no. 3 (2018): 313-329.

[66.] Dai, Jinhua, Anton W. Jensen, Dillip K. Mohanty, Jason Erndt, and Merlin L. Bruening. "Controlling the permeability of multilayered polyelectrolyte films through derivatization, cross-linking, and hydrolysis." *Langmuir* 17, no. 3 (2001): 931-937.

[67.] Khan, M. Z. H. "Nanoparticles modified ITO based biosensor." *Journal of Electronic Materials* 46, no. 4 (2017): 2254-2268.

[68.] Lide, David R., ed. *CRC handbook of chemistry and physics*. Vol. 85. CRC press, 2004.

[69.] Shih, Kaimin. *X-ray diffraction: Structure, principles and applications*. Nova Science Publishers, Inc., 2013.

[70.] Kim, Seong H., Christopher M. Lee, and Kabindra Kafle. "Characterization of crystalline cellulose in biomass: Basic principles, applications, and limitations of XRD, NMR, IR, Raman, and SFG." *Korean Journal of Chemical Engineering* 30 (2013): 2127-2141.

[71] Ali, Asif, Yi Wai Chiang, and Rafael M. Santos. "X-ray diffraction techniques for mineral characterization: A review for engineers of the fundamentals, applications, and research directions." *Minerals* 12, no. 2 (2022): 205.

[72.] Singh, Jung Bahadur. "Phases in Alloy 625." In *Alloy 625: Microstructure, Properties and Performance*, pp. 29-65. Singapore: Springer Nature Singapore, 2022.

[73.] Akhtar, Kalsoom, Shahid Ali Khan, Sher Bahadar Khan, and Abdullah M. Asiri. *Scanning electron microscopy: Principle and applications in nanomaterials characterization*. Springer International Publishing, 2018.

[74.] Kannan, M. "Scanning electron microscopy: Principle, components and applications." *A textbook on fundamentals and applications of nanotechnology* (2018): 81-92.

[75.] Hayes, T. L., and R. F. W. Pease. "The scanning electron microscope: principles and applications in biology and medicine." *Advances in biological and medical physics* 12 (1968): 85-137.

[76.] Profeta, William Henrique Silva, Otto Haubrich, Jonnathan Toshio Ogihara, Gabriel Garro Gomes Fontes, Itamar Arnaldo Tororó Pereira, Ary Machado de Azevedo, Joana Batista Soares, Edson Ramos de Andrade, and Domingos D'Oliveira Cardoso. "Radiometric survey in microscopy laboratory." *Brazilian Journal of Radiation Sciences* 11, no. 1A (Suppl.) (2023): 1-10.

[77.] Nicolet, Thermo, and C. All. "Introduction to fourier transform infrared spectrometry." *Thermo Nicolet Corporation* (2001).

[78.] Saptari, Vidi. *Fourier transform spectroscopy instrumentation engineering*. Bellingham Washington, DC: SPIE Optical Engineering Press, 2003

[79.] Griffiths, P. R., and J. A. De Haseth. "Fourier Transform Infrared Spectrometry John Wiley & Sons." *New York* 340 (1986).

[80.] Ferraro, John R., and Louis J. Basile, eds. *Fourier transform infrared spectra: applications to chemical systems*. Academic press, 2012.

[81.] Verma, Govinda, and Manish Mishra. "Development and optimization of UV-Vis spectroscopy-a review." *World J. Pharm. Res* 7, no. 11 (2018): 1170-1180.

[82.] Mukadam, M., N. A. M. Khan, S. Khan, and A. Kauchali. "Uv–vis spectroscopy in analysis of phytochemicals." *Int. J. Pharm. Res. Appl.* 6 (2021): 482-499.

[83.] MAJEED, Mahmood Hameed. "THE INVESTIGATION OF DOPING EFFECTS ON FORBIDDEN BAND GAP VALUE OF ZnO: EXPERIMENTAL AND THEORETICAL STUDIES."

[84.] Stoica, Daniela, Paul J. Brewer, Richard JC Brown, and Paola Fisicaro. "Influence of fabrication procedure on the electrochemical performance of Ag/AgCl reference electrodes." *Electrochimica acta* 56, no. 27 (2011): 10009-10015.

[85.] Van Benschoten, James J., Jane Y. Lewis, William R. Heineman, Daryl A. Roston, and Peter T. Kissinger. "Cyclic voltammetry experiment." *Journal of Chemical Education* 60, no. 9 (1983): 772.

[86.] Parthasarathy, P., and S. Vivekanandan. "Biocompatible TiO2-CeO2 nano-composite synthesis, characterization and analysis on electrochemical performance for uric acid determination." *Ain Shams Engineering Journal* 11, no. 3 (2020): 777-785.

[87.] Barbosa, José, and Victoria Sanz-Nebot. "Standard pH values for phosphate buffer reference solutions in acetonitrile-water mixtures up to 50%(m/m)." *Microchimica Acta* 116 (1994): 131-141.

[88.] Ammar, I. A., S. A. Darwish, M. W. Khalil, and S. El-Taher. "Kinetics of the ferro—ferricyanide electron transfer reaction on anodically formed tin oxide." *Electrochimica acta* 33, no. 2 (1988): 231-238.

[89.] Evans, Dennis H., Kathleen M. O'Connell, Ralph A. Petersen, and Michael J. Kelly. "Cyclic voltammetry." (1983): 290.

[90.] Yamada, Hirohisa, Kazuki Yoshii, Masafumi Asahi, Masanobu Chiku, and Yuki Kitazumi. "Cyclic Voltammetry Part 1: Fundamentals." *Electrochemistry* 90, no. 10 (2022): 102005-102005.

[91.] Van Benschoten, James J., Jane Y. Lewis, William R. Heineman, Daryl A. Roston, and Peter T. Kissinger. "Cyclic voltammetry experiment." *Journal of Chemical Education* 60, no. 9 (1983): 772.

[92.] Khan, Muhammad Salman, Afia Asif, Saed Khawaldeh, and Ahmet Tekin. "Dopamine detection using mercaptopropionic acid and cysteamine for electrodes surface modification." *Journal of Electrical Bioimpedance* 9, no. 1 (2018): 3-9.

[93.] Lee, Junqiao. "Electrochemical sensing of oxygen gas in ionic liquids on screen printed electrodes." PhD diss., Curtin University, 2014.

[94.] Liu, Jingjing, Yifei Xu, Shikun Liu, Shixin Yu, Zhirun Yu, and Sze Shin Low. "Application and progress of chemometrics in voltammetric biosensing." *Biosensors* 12, no. 7 (2022): 494.

[95.] Wang, H. Y., M. L. Pan, Y. L. Oliver Su, S. C. Tsai, C. H. Kao, S. S. Sun, and W. Y. Lin. "Comparison of Differential Pulse Voltammetry (DPV)—a new method of carbamazepine analysis—with Fluorescence Polarization Immunoassay (FPIA)." *Journal of Analytical Chemistry* 66 (2011): 415-420.

[96.] Palma, Alberto, Mercedes Ruiz Montoya, Jesús F. Arteaga, and Jose M. Rodríguez Mellado. "Determination of antioxidant activity of spices and their active principles by differential pulse voltammetry." *Journal of agricultural and food chemistry* 62, no. 3 (2014): 582-589.

[97.] Knowledege Base, Plamsens *Potential applied during the Differential Pulse Voltammetry* [Online image] [Accessed on 19th May 2024] https://www.palmsens.com/knowledgebase-article/differential-pulse-voltammetry-dpv/

[98.] Disale, Sujit D., and Shivram S. Garje. "A convenient synthesis of nanocrystalline chalcopyrite, CuFeS2 using single-source precursors." *Applied Organometallic Chemistry* 23, no. 12 (2009): 492-497

[99.] Nsude, Hope E., Kingsley U. Nsude, Goodfriend M. Whyte, Raphael M. Obodo, Chinedu Iroegbu, M. Maaza, and Fabian I. Ezema. "Green synthesis of CuFeS 2 nanoparticles using mimosa leaves extract for photocatalysis and supercapacitor applications." *Journal of Nanoparticle Research* 22 (2020): 1-13.

[100.] Ntelane, Tau S., Usisipho Feleni, Nomcebo H. Mthombeni, and Alex T. Kuvarega. "Cufes2 Supported on Dendritic Mesoporous Silica-Titania (Dmst) for Persulfate-Assisted Degradation of Sulfamethoxazole Under Visible Light." *Available at SSRN 4500206*

[101.] Bastola, Ebin, Khagendra P. Bhandari, Indra Subedi, Nikolas J. Podraza, and Randy J. Ellingson. "Structural, optical, and hole transport properties of earth-abundant chalcopyrite (CuFeS2) nanocrystals." *MRS Communications*

[102.] Prameena, B., G. Anbalagan, S. Gunasekaran, G. R. Ramkumaar, and B. Gowtham. "Structural, optical, electron paramagnetic, thermal and dielectric characterization of chalcopyrite." *Spectrochimica Acta Part A: Molecular and Biomolecular Spectroscopy* 122 (2014): 348-355.

[103.] da Silveira Salla, Julia, Guilherme Luiz Dotto, Dachamir Hotza, Richard Landers, Katia da Boit Martinello, and Edson Luiz Foletto. "Enhanced catalytic performance of CuFeS2 chalcogenide prepared by microwave-assisted route for photo-Fenton oxidation of emerging pollutant in water." *Journal of Environmental Chemical Engineering* 8, no. 5 (2020): 104077

[104.] Liu, Zezhong, Zengxu Liu, Zhen Zhao, Danxia Li, Pengfei Zhang, Yanfang Zhang, Xiangyong Liu, Xiaoteng Ding, and Yuanhong Xu. "Photothermal regulated nanozyme of CuFeS2 nanoparticles for efficiently promoting wound healing infected by multidrug resistant bacteria." *Nanomaterials* 12, no. 14 (2022): 2469

[105.] Elgrishi N, Rountree KJ, McCarthy BD, Rountree ES, Eisenhart TT, Dempsey JL (2018) A practical beginner's guide to cyclic voltammetry. J Chem E

# Appendix- I: Plagiarism Report

● **8% Overall Similarity**

Top sources found in the following databases:

- 4% Internet database
- Crossref database
- 5% Submitted Works database

- 2% Publications database
- Crossref Posted Content database

TOP SOURCES

The sources with the highest number of matches within the submission. Overlapping sources will not be displayed.

| | | |
|---|---|---|
| **1** | **link.springer.com**<br>Internet | **<1%** |
| **2** | **ncbi.nlm.nih.gov**<br>Internet | **<1%** |
| **3** | **Aligarh Muslim University, Aligarh on 2023-08-12**<br>Submitted works | **<1%** |
| **4** | **Nitin K. Puri, Kanika Sharma. "Enhanced Electrochemical Performance ...**<br>Crossref | **<1%** |
| **5** | **Indiana University on 2023-11-06**<br>Submitted works | **<1%** |
| **6** | **University of Southampton on 2023-03-24**<br>Submitted works | **<1%** |
| **7** | **Queen Mary and Westfield College on 2023-08-13**<br>Submitted works | **<1%** |
| **8** | **University of New South Wales on 2012-01-05**<br>Submitted works | **<1%** |

Sources overview

Sources overview

21 Yongdeuk Hwang, Yurim Kim, Jiin Min, Jinmyung Jung. "Identification ... <1%
Crossref

22 journals.tubitak.gov.tr <1%
Internet

23 Nazarbayev University on 2024-04-29 <1%
Submitted works

24 SUNY Brockport on 2016-02-12 <1%
Submitted works

25 rockymountainlabs.com <1%
Internet

26 Higher Education Commission Pakistan on 2024-03-23 <1%
Submitted works

27 Sydney Boys High School on 2023-12-30 <1%
Submitted works

28 The Robert Gordon University on 2020-01-27 <1%
Submitted works

29 ebin.pub <1%
Internet

30 mdpi.com <1%
Internet

31 National University of Singapore on 2012-04-30 <1%
Submitted works

32 Universiti Teknologi Malaysia on 2011-07-04 <1%
Submitted works

# Certificate

ICAMNOP 2023- Abstract Status - arun_2k22mscphy05@dtu.ac.in - Delhi Technological University Mail - Person 1 - Microsoft Edge

https://mail.google.com/mail/u/1/popout?ver=1gkk8ieoozcsz&search=inbox&th=%23thread-f%3A1783972237475995841&cvid=1

## ICAMNOP 2023- Abstract Status  Inbox ×

**ICAMNOP 2023 DTU** <icamnop@dtu.ac.in>                                      Thu, Nov 30, 2023, 12:45 PM
to me ▾

Dear Mr. Arun Saji,

Warm greetings from the ICAMNOP 2023 (International Conference on Atomic, Molecular, Material, Nano and Optical Physics with Applications)!

We are pleased to inform you that your abstract **ABS54 " Hydrothermal Synthesis and Characterization of Nanocomposite based on Chalcopyrite Nanostructures decorated Hexagonal Boron Nitrides Nanosheets to Investigate the Electrochemical Sensing of NSCLC Biomarker"** has been accepted for a **poster** presentation at the ICAMNOP 2023 Conference.

We are thrilled to have you participate in this exciting conference, which is scheduled to take place in Delhi, India from 20th to 22nd December 2023. With an incredible lineup of technical presentations and discussions, we are confident that ICAMNOP 2023 will be a memorable and enriching experience, and you will benefit greatly from this platform.

The details for registration to the conference can be found at https://icamnop.in/registration. Please remember that Early Bird Registration ends on 30th November 2023.

We look forward to seeing you at ICAMNOP Conference.

--
Warm Regards
**Prof. Vinod Singh**
Convener, ICAMNOP-2023 &
Professor, Department of Applied Physics
Delhi Technological University (DTU),
Shahbad Daulatpur, Bawana Road, Delhi-110042, India
Email: vinodsingh.iitd12@gmail.com, vinodsingh@dtu.ac.in

Conference website : https://www.icamnop.in/

55